# Magma-Mush Interactions in the Lower Oceanic Crust: Insights From Atlantis Bank Layered Series (Southwest Indian Ridge)

M. Boulanger, L. France, C. Ferrando, Benoit Ildefonse, B. Ghosh, A. Sanfilippo, C.-z. Liu, T. Morishita, J. Koepke, O. Bruguier

JGR Solid Earth

RESEARCH ARTICLE
10.1029/2021JB022331

# Magma-Mush Interactions in the Lower Oceanic Crust: Insights From Atlantis Bank Layered Series (Southwest Indian Ridge)

**M. Boulanger[1,2], L. France[1], C. Ferrando[1,3], B. Ildefonse[4], B. Ghosh[5], A. Sanfilippo[3], C.-Z. Liu[6], T. Morishita[7], J. Koepke[2], and O. Bruguier[4]**

[1]Université de Lorraine, CNRS, CRPG, Nancy, France, [2]Institut für Mineralogie, Leibniz Universität Hannover, Hannover, Germany, [3]Dipartimento di Scienze della Terra e dell'Ambiente, Università degli Studi di Pavia, Pavia, Italy, [4]Géosciences Montpellier, Université de Montpellier, CNRS, Montpellier, France, [5]Department of Geology, University of Calcutta, Kolkata, India, [6]State Key Laboratory of Lithospheric Evolution, Institute of Geology and Geophysics, Chinese Academy of Sciences, Beijing, China, [7]College of Science and Engineering, Kanazawa University, Kanazawa, Japan

**Abstract** Magma migration and differentiation processes are key to understanding the development and evolution of oceanic magma reservoirs. To provide new quantitative geochemical constraints on these processes, we applied a high-resolution approach to study an interlayered section of the lower oceanic crust sampled at Atlantis Bank, on the (ultra)slow-spreading Southwest Indian Ridge. The section is characterized by sharp grain-size layering between fine- and coarse-grained olivine gabbros that is representative of other layered structures described at the Atlantis Bank oceanic core complex. The textures and fabrics of the layers and the nature of their contacts indicate formation by intrusion of a magma (i.e., crystal-bearing) into an almost solidified coarse-grained mush. Petrographic observations and *in situ* incompatible trace element signatures indicate that the fine- and coarse-grained layers record reactive porous migration of melts. Widespread reactive porous flow occurred prior to intrusion within the coarse-grained gabbro, producing mineral compositions enriched in incompatible elements. The intrusive fine-grained lithology records a late stage event of localized reactive melt percolation in cm-scale structures, which lead to strong light rare earth elements depletion relative to heavy rare earth elements. In addition, we highlight the occurrence of interactions at the contacts between layers and partial modification in compositions of the intruded lithology. This layered section likely represents a contact between two larger magma bodies emplaced within the lower crust during accretion, where the type of melt migration (intrusion or porous flow) and the modalities of melt percolation (widespread or localized) strongly govern the composition of the crustal lithologies.

**Plain Language Summary** We present the study of a 1m35 borehole section of oceanic crust exhumed at Atlantis Bank on the Southwest Indian Ridge. This section presents characteristic layering defined by successive fine- and coarse-grained olivine gabbro layers, which recorded the conditions and modalities of magma emplacement and evolution during oceanic crust accretion. We conducted a high-resolution study of samples collected continuously along the section, including a description of the petrography, analysis of microstructures, and geochemistry of both rocks and minerals. This high-resolution approach allowed us to reconstruct the intricate formation steps of the section, which involves the two main melt migrations processes at depth: an intrusion, represented by the fine-grained layers, and porous melt flow, which occurs at all steps of formation of the lithologies. The latter process strongly impacted the textures and composition of the lithologies. These compositions provide information on the modalities of the porous melt migration, which can be pervasive or focused in discrete structures. The geometry of the layer contacts together with the emplacement model suggests that this layering likely represents an irregular contact between two larger intrusions or magma reservoirs emplaced within the oceanic crust.

**Key Points:**

- At slow-spreading ridges, igneous layering in the lower crust records intrusive events of crystal-bearing magmas
- At lower crustal levels, melt migration proceeds by intrusion and reactive porous flow
- Melt migration modes strongly influence the chemical compositions of melts, crystal matrices, and crustal lithologies

**Supporting Information:**

Supporting Information may be found in the online version of this article.

**Correspondence to:**

M. Boulanger,
mgeoblg@gmail.com

**Citation:**

Boulanger, M., France, L., Ferrando, C., Ildefonse, B., Ghosh, B., Sanfilippo, A., et al. (2021). Magma-mush interactions in the lower oceanic crust: Insights from Atlantis Bank layered series (Southwest Indian Ridge). *Journal of Geophysical Research: Solid Earth*, *126*, e2021JB022331. https://doi.org/10.1029/2021JB022331

Received 29 APR 2021
Accepted 18 AUG 2021



## 1. Introduction

The main igneous processes responsible for the oceanic crust accretion, which is responsible for the formation of ~70% of the Earth's surface, have been primarily ascribed to equilibrium and fractional crystallization

of mantle melts. Both processes have been characterized and quantified based on natural samples (e.g., O'Hara, 1965; Ross & Elthon, 1997; Natland & Dick, 2001; Sanfilippo & Tribuzio, 2013), or reproduced and constrained by experimental petrology (e.g., Feig et al., 2010; Husen et al., 2016; Villiger, Müntener, & Ulmer, 2007; Villiger, Ulmer, & Müntener, 2007) and by numerical modeling (e.g., Coogan et al., 2001; Meyer et al., 1989). However, the developing vision of oceanic magma reservoirs as mush-dominated environments, and new comprehensive petrologic and geochemical studies of crustal and mantle lithologies have highlighted that melt-rock or melt-mush reactions triggered by reactive porous flow (RPF) potentially exerts a major control on both lower and upper crustal compositions (e.g., Basch et al., 2019; Bédard et al., 2000; Collier & Kelemen, 2010; Coogan et al., 2000; Dick, Schouten, et al., 1991; Drouin et al., 2009; Ferrando et al., 2018; Gao et al., 2007; Leuthold et al., 2018; Lissenberg & MacLeod, 2016; Rampone et al., 2008; Sanfilippo et al., 2015; Suhr et al., 2008).

The modalities of melt migration and storage within the accreting crust at slow-spreading ridges, which in turn controls melt evolution processes, remain not sufficiently constrained. Only a few seismic imaging studies have reported the presence of melt at depth (Canales et al., 2017; Jian et al., 2017; Magde et al., 2000; Singh et al., 2006; Sinha et al., 1997, 1998) in environments where magma inputs form the mantle is considered relatively low (e.g., Dick et al., 2003; Rubin & Sinton, 2007; except for Sinha et al., 1998 and the Reykjanes ridge). Melt at slow-spreading ridges migrates either by magmatic intrusion (e.g., Canales et al., 2017; Dick, Schouten, et al., 1991; Dunn et al., 2005) or by RPF (e.g., Coogan et al., 2000; Ferrando, France, et al., 2021; Sanfilippo et al., 2020; Zhang et al., 2021). Sill intrusions and stacking is likely central in the accretion of the least evolved sections recovered at slow-spreading centers (Bédard, 2015; Boulanger et al., 2020; Godard et al., 2009; Grimes et al., 2008; Sanfilippo & Tribuzio, 2013). Evidences of reaction between a percolating melt and the surrounding rock or mush have been identified in various localities in slow-spreading crust (Boulanger et al., 2020; Ferrando, France, et al., 2021; Lissenberg & MacLeod, 2016; Lissenberg et al., 2019; Sanfilippo et al., 2020). Variations in the intensity of those reactions resulting from RPF have been proposed to account for the first-order differences reported for deep crustal sections (e.g., gabbros at Atlantis Massif, olivine gabbros at Atlantis Bank; Dick, MacLeod, et al., 2019). Also, some of the olivine-rich troctolites recovered in fossil oceanic crust (e.g., Basch et al., 2019; Sanfilippo et al., 2014) and drilled in the Atlantis Massif oceanic core complex (OCC; Drouin et al., 2009; Ferrando et al., 2018; Suhr et al., 2008) likely result from interactions of percolating melts with an olivine-rich matrix of mantle origin. At Atlantis Bank, the strong control exerted by RPF on melt differentiation was shown at the scale of a thin section (Sanfilippo et al., 2020) as well as at the scale of an entire magma reservoir or lower crust (Boulanger et al., 2020; Zhang et al., 2021). In addition, widespread textural and geochemical evidences for RPF were found at various crustal levels and up to the latest magma evolution stages (Gao et al., 2007; Leuthold et al., 2018; Lissenberg & Dick, 2008; MacLeod et al., 2017a; Natland et al., 1991; Nguyen et al., 2018; Sanfilippo et al., 2015).

We study here one of the recurrent petrographic features found in the lower crust drilled at Atlantis Bank: Grain-size variations in olivine gabbros that can take the form of irregular patches of fine-grained material within the host coarse-grained lithology, or alternation between fine- and coarse-grained layers of gabbros s.l. (*sensu lato*; Bloomer et al., 1991; Dick, MacLeod, et al., 2019; Dick, Schouten, et al., 1991; Ferrando, France, et al., 2021; MacLeod et al., 2017a; Natland & Dick, 2002; Niu et al., 2002). The first type (irregular patches) that is present in average every 4 m in IODP Hole U1473A, was explored by Ferrando, France, et al. (2021), and shown to be related to the extraction and collection of reacted interstitial melts from coarse-grained mushy domains to form the fine-grained patches. We hereafter focus on the second type of discrete layered structures, which shows only subtle modal changes between layers. Layering *sensu stricto* is defined as an "overall structure of cumulates which develops through the combination of individual layers, each forming sheet-like cumulate units and each being a distinctive entity in its compositional and/or textural features" (Irvine, 1982; Naslund & McBirney, 1996; Namur et al., 2015). This definition, which does not involve a specific formation process, applies here to the structures found at Atlantis Bank as described at the scale of the cores section (6 cm in diameter). Layering has been heavily studied in various plutonic bodies from continental and oceanic environments, and provides key information on the igneous and structural processes involved in magma body accretion. Layering can originate from internal processes to magma reservoirs such as crystal settling and related gravitational sorting, variations in nucleation and growth rates, and compaction (Namur et al., 2015 and references therein; Mock et al., 2020). Layering formation can also be linked to intrusive events (Holness et al., 2007; Tegner et al., 1993), or to tectonic deformation of magma

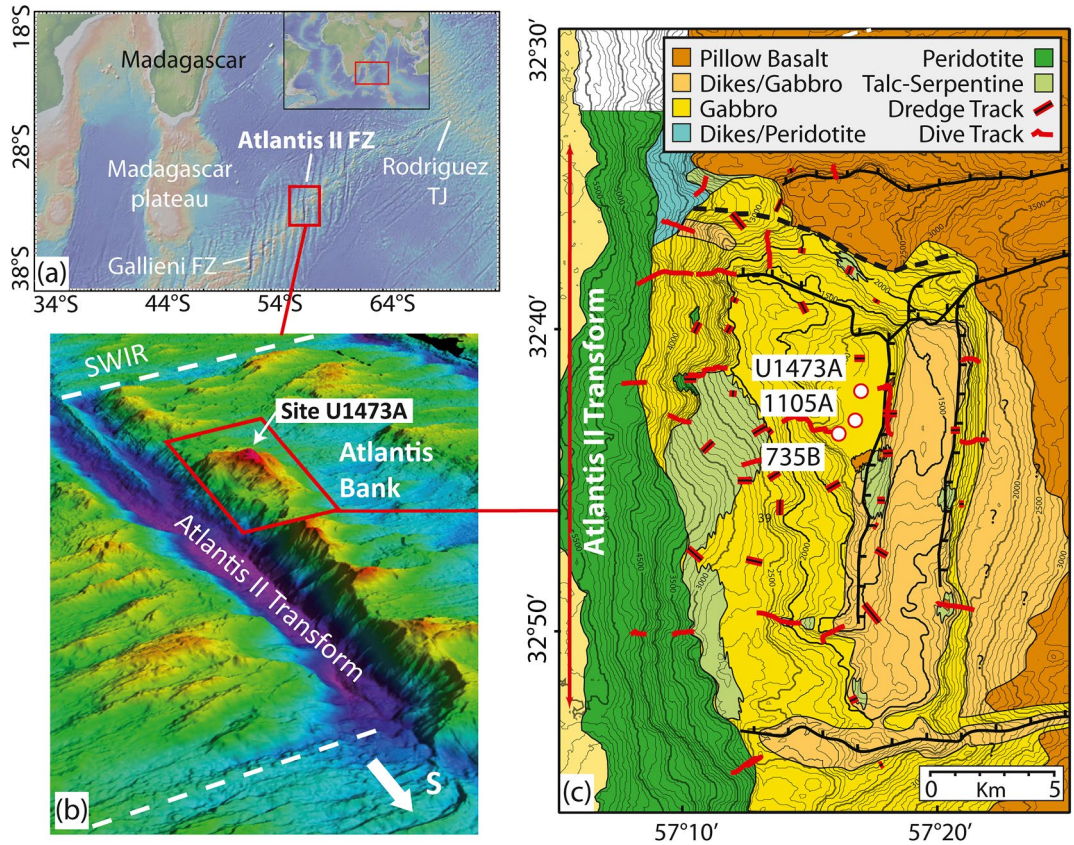


**Figure 1.** (a) Location map of the Atlantis II Fracture Zone (from Ryan et al., 2009), (b) 3D bathymetric map of the Atlantis II Fracture Zone and location of the Atlantis Bank oceanic core complex (OCC) (MacLeod et al., 2017b), and (c) Geological map of the Atlantis Bank OCC and location of ODP/IODP Holes 735B, 1105A, and U1473A (Dick, Kvassnes, et al., 2019). White area: not references.

bodies in domains like mid-ocean ridges (Bédard, 2015; Higgie & Tommasi, 2012; Jousselin et al., 2012; Quick & Denlinger, 1993). Alternatively, crystal-plastic deformation can overprint initial magmatic layering that potentially acted as a planar anisotropy to favor deformation (MacLeod et al., 2017a), thus altering the record of magmatic layering. In slow-spreading environments, discrete layering has been described in both ophiolites (Corsican, Alpine and Ligurian ophiolites: Lagabrielle et al., 2015; Sanfilippo & Tribuzio, 2011, 2013) and in present day oceanic crust (at OCCs, Blackman et al., 2006; Dick et al., 2000). The study of magmatic layering from lower oceanic crust therefore has the potential to record key magmatic processes involved in their formation, such as melt migration processes ongoing during crustal accretion.

## 2. Geological Settings

OCCs at slow-spreading ridges represent exhumation of lower crust and mantle sections by detachment faulting during asymmetric spreading, and provide an invaluable opportunity to study deep crustal sections (Cann et al., 1997; Escartín et al., 2008; Ildefonse et al., 2007; Lagabrielle et al., 2015). The Atlantis Bank OCC locates along the Southwest Indian Ridge, on the eastern wall of the Atlantis II Fracture Zone (Figures 1a and 1b). The OCC formed as a consequence of a 3 km uplift of lower crustal gabbros (Dick, Meyer, et al., 1991), which results from the offset of a detachment fault (of about 1 km) from transform-parallel normal faults during a period of change in the spreading direction at the ridge axis ~19.5 Ma (Baines et al., 2003). Baines et al. (2008) have quantified a half-spreading rate during detachment faulting of ~1.4 cm/yr (ultraslow-spreading ridge). Three deep holes were drilled by the ODP/IODP at Atlantis Bank: ODP Hole 735B (deepest with a total depth of 1,508 m below sea floor, mbsf; Dick et al., 2000); ODP Hole 1105A, located 1.4 km north of hole 735B (158 mbsf; Casey et al., 2007; MacLeod et al., 2017b); IODP Hole

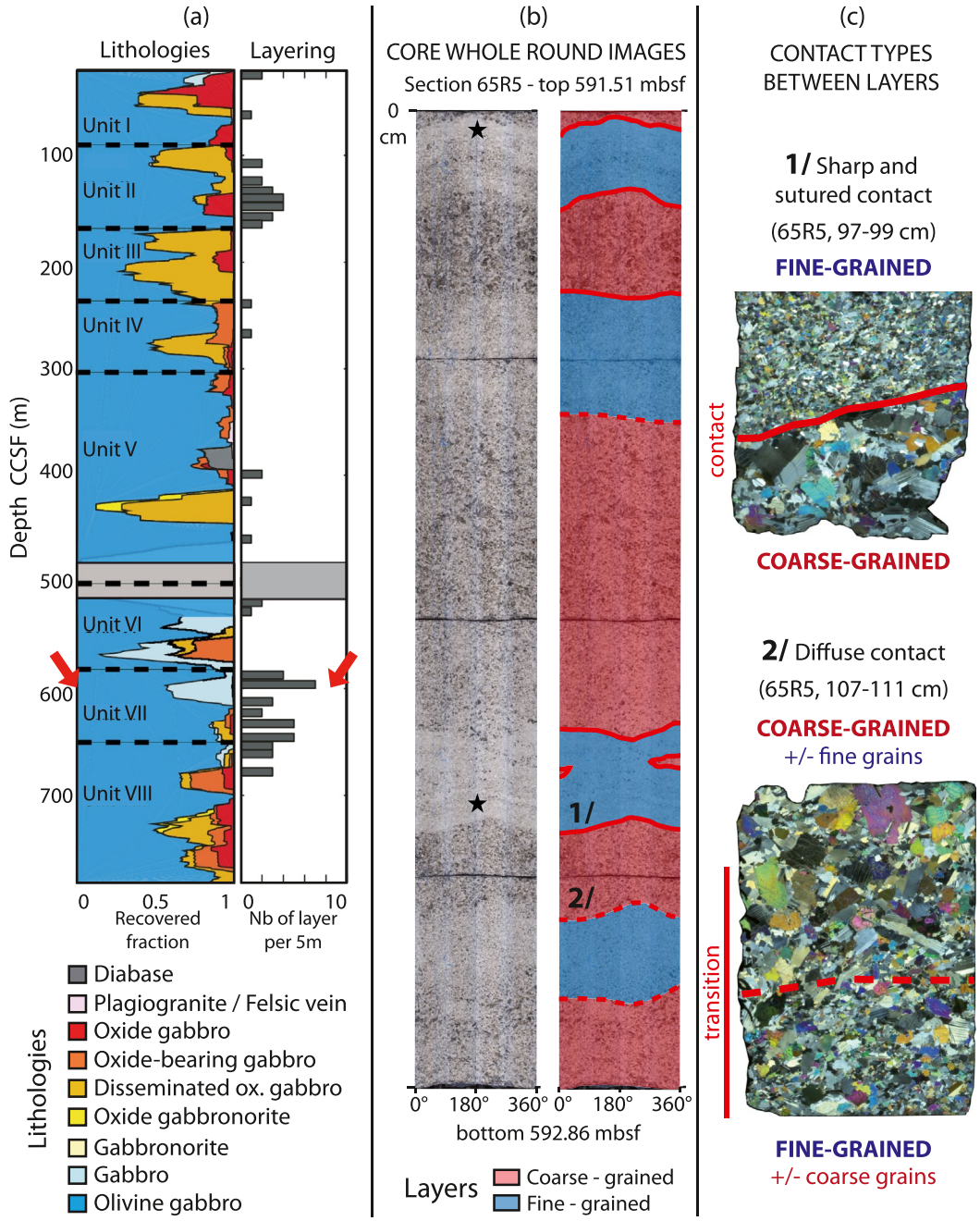


**Figure 2.** (a) Lithostratigraphic variations of IODP Hole U1473A (modified from Dick, MacLeod, et al., 2019). Relative abundances are averaged over 20 m, dashed lines represent unit boundaries, and the histogram documents the number of igneous layers identified every 5 m. Red arrows indicate the depth of section U1473A-65R5 (~592–593 mbsf, shown in panel b). (b) Whole round images of section U1473A-65R5 (top and bottom depths indicated on both sides). Red lines indicate boundaries between coarse- (red) and fine-grained (blue) layers. Black stars: Location of the finer grained bands. 1/ and 2/ indicate the location of the layer contacts presented in panel (c). (c) Thin section scans (2 cm width) in plane polarized light of typical sharp (1/) and diffuse (2/) contacts as identified in the section.

U1473A, located 2.2 km north-northeast of hole 735B (809 mbsf; Dick, MacLeod, et al., 2019; MacLeod et al., 2017a; Figure 1c). The three sections share very similar petrographic features and present the same highly variable lithological assemblages. Lithologies range from primitive troctolites to more differentiated oxide gabbros, with olivine gabbros representing most of the cored sections (68% of ODP Hole 735B and 76.5% of IODP Hole U1473A, Figure 2a; Dick et al., 2002; MacLeod et al., 2017a).

Together with modal mineralogy, grain size, texture, magnetic susceptibility, geochemical composition, and lithological distribution, the presence of layering constitutes one of the main parameters used to identify lithological units (MacLeod et al., 2017a). Layering is rather sparse in Atlantis Bank sections, with only localized meter-thick layered intervals (MacLeod et al., 2017a, 2017b; Natland & Dick, 2002). In hole U1473A, eight lithological units were described and sparse layering occurs in almost every ones (Figure 2a; Dick, MacLeod, et al., 2019). Relatively intense layering is present in two units: Unit II with a strong crystal-plastic deformation overprint (between 100 and 175 mbsf with up to four layers per 5 m) and Unit VII (between 578 and 642 mbsf with up to seven layers per 5 m). Layering is characterized by contrasting grain size, ranging from fine- to coarse-grained material, and only few layering present weak variations in modal mineralogy. Most of the contacts between layers are sub-planar and sharp, and are only locally slightly diffuse or gradational (~10% of the contacts between layers). The layering fabric is commonly overprinted by crystal-plastic deformation, preventing any reliable study of the initial magmatic processes involved. Locally, deformation is too intense to identify if any initial magmatic (mineralogical or textural) heterogeneity was present before deformation (MacLeod et al., 2017b), hence the amount of magmatic layering in the hole is likely underestimated.

Hereafter, we consider a 1.35 m-long layered section from the main layered unit of Hole U1473A sampled at 590 mbsf (Unit VII; Figure 2b). We conducted high-resolution petrologic, geochemical, and structural studies of the successive fine- and coarse-grained layers to identify the origin of the layering and discuss melts migration, crystallization, and potential melt-mush interaction processes occurring within the lower crust.

## 3. Analytical Methods

### 3.1. Electron Backscatter Diffraction (EBSD)

Details on EBSD measurements and data processing are presented in Text S1 in addition to the data (Table S1). The parameters based on EBSD measurements used to describe the microstructures of the studied samples are presented hereafter.

Intragrain misorientation is quantified as the angle between the crystallographic orientation of a particular pixel within a grain and the average orientation of all pixels of the same grain (Mis2Mean parameter). The grain orientation spread (GOS) is the average of the Mis2Mean and the average GOS quantifies the grain misorientation per sample. The fabric strength and distribution density of the principle crystallographic axes are determined by calculating the *J* index (e.g., Mainprice & Silver, 1993) of the orientation distribution function (ODF); *J* varies from 1 for a random distribution to infinity for a single perfectly uniform crystal. We calculated the ODF using the "de la Vallee Poussin" kernel with a half-width of 10° (Mainprice et al., 2014). The symmetry of the mineral crystal preferred orientations (CPOs) is evaluated by calculating the BA (for plagioclase) and BC indexes (for olivine and clinopyroxene—Satsukawa et al., 2013; Mainprice et al., 2014). The BA and BC indexes are based on three other indexes *P*, *G*, and *R* (Point, Girdle and Random). The three indexes are calculated using the eigenvalues of the orientation tensor that represent the distribution of the crystallographic axes (or poles to crystallographic planes) in each pole figure (Satsukawa et al., 2013). BA and BC indexes vary between 0 and 1, and represent the relative weight of the fabrics defined by (100) and (010) for the former, and (010) and (001) for the latter, and thus the predominance of lineation with high BA and BC or foliation with low BA and BC.

For non-equigranular samples, coarse grains are overrepresented in pole figures when calculating the ODF from the orientations of each pixel. To avoid this bias, we instead used the average orientations of the grains (one-point-per-grain data, 1PPG) to calculate the ODF. In this study, we used individual EBSD maps of coarse-grained samples to discuss misorientation data, but the small number of grains analyzed makes these maps statistically irrelevant to discuss orientations and fabrics (less than 20 olivine [Ol] grains and less than 50 plagioclase [Pl] grains without considering sparse recrystallized grains at grain boundaries). To increase the number of minerals analyzed, 1PPG data for eight coarse-grained material maps were concatenated with the Channel 5 software suite and similarly processed as an individual map (Figure S1).

### 3.2. Whole Rock Major and Trace Element Analyses

Major and trace elements concentrations of each layer of the section (four finer- and three coarser-grained lithologies) were measured by the Service d'Analyses des Roches et des Minéraux (CRPG, Nancy, France) via inductively coupled plasma optical emission spectrometry and inductively coupled plasma mass spectrometry (ICP-MS), respectively. Details on analytical protocols and data are given in Text S2 and Table S2.

### 3.3. Electron Probe Microanalysis (EPMA)

*In situ* major element contents of Ol, Pl and clinopyroxene (Cpx) were quantified by EPMA at the Laboratoire Magmas et Volcans (Clermont-Ferrand, France) with a Cameca SX100 equipped with four wavelength dispersive X-ray spectrometers. Analyses for all minerals were performed with a 15 kV accelerating potential and a focused beam using a 15 nA beam current. On-peak and background counting times were 10 or 20 s (see details and calibration standards for each element in Table S3). The data and associated analytical errors are available in Table S3.

### 3.4. Laser Ablation Inductively Coupled Plasma Mass Spectrometry (LA-ICP-MS)

*In situ* trace element contents of minerals were analyzed with a ThermoFinnigan Element2 XR ICP-MS coupled with a Microlas-GeoLas Q+ housing a Lambda-Physik CompEx 102 excimer laser at Géosciences Montpellier (AETE-ISO regional facility of the OSU OREME, Montpellier University, France). Signal acquisition was performed in time-resolved acquisition mode, counting 2 min for blanks and 1 min for sample measurements. The laser frequency was 8 Hz with an energy density of ~12–15 J $cm^2$. Ablation was performed in He gas, which was mixed with Ar before entering the plasma. Cpx was analyzed with a laser spot size of 77 μm, whereas a spot size of 102 μm was used for Ol and Pl. Data were processed using the GLITTER software (van Achterbergh et al., 2004). All measured concentrations were calibrated to the synthetic glass NIST 612 using the values of Pearce et al. (1997). Internal standards used for the minerals were $^{43}Ca$ for Cpx and $^{29}Si$ for Pl and Ol, previously measured for each point by EPMA. The averaged values (and associated 2SD values) obtained by LA-ICP-MS analyses of the standard reference basalt BIR-1G are available in Table S4, together with all trace element data and associated analytical errors.

## 4. Results—Characteristics of the Layered Section

### 4.1. Lithologies and Contacts

We focus on the interval at ~592–593 mbsf in Unit VII of IODP Hole U1473A, where the layer frequency is highest (section 65R5, Figures 2a and 2b) and very well preserved (i.e., no alteration or strong crystal-plastic deformation; MacLeod et al., 2017a). Macroscopically the 1.35-m-long section 65R5 shows seven successive fine- and coarse-grained layers (average grain sizes of ~0.5 and ~5 mm, respectively) of olivine gabbros. The average thickness of the layers is of 13 cm for the fine-grained (between 8 and 16 cm thick) and ~20 cm for the coarse-grained layers (between 10 and 40 cm thick; Figure 2b). The section was continuously sampled except for the center of the thickest coarse-grained layer (between 54 and 72.4 cm from the top of the section), where two samples collected between 63 and 69 cm depth are available. There is no systematic change in modal composition between the fine- and coarse-grained layers, which contain on average 58% Pl (58% in both cases), 28% Cpx (29% and 26%, respectively) and 8% Ol (6% and 10%, respectively) as quantified by EBSD measurements. Other identified minerals are orthopyroxenes (2% in average), and less than 1% accessory minerals (brown amphibole, ilmenite and magnetite, and sulfides—mostly pyrites with some chalcopyrites and pentlandite).

Coarse-grained olivine gabbro presents granular to subophitic textures. Pl are elongate subhedral to anhedral crystals. They present well developed mechanical twins, and the longest crystal laths are often bent (Figure 3a). Most Pl show irregular and corroded boundaries with surrounding minerals, and are present as small corroded chadacrysts in Cpx or other Pl (identified by a difference in twins presence and orientation; Figures 3b and 3d). Ol are mostly anhedral to subhedral and deformed, with the presence of well-developed kink bands in the largest minerals (Figure 3f). They show irregular and corroded grain boundaries at the contacts with Pl and Cpx (Figures 3a and 3f). When present as chadacrysts within Pl or Cpx, Ol form small

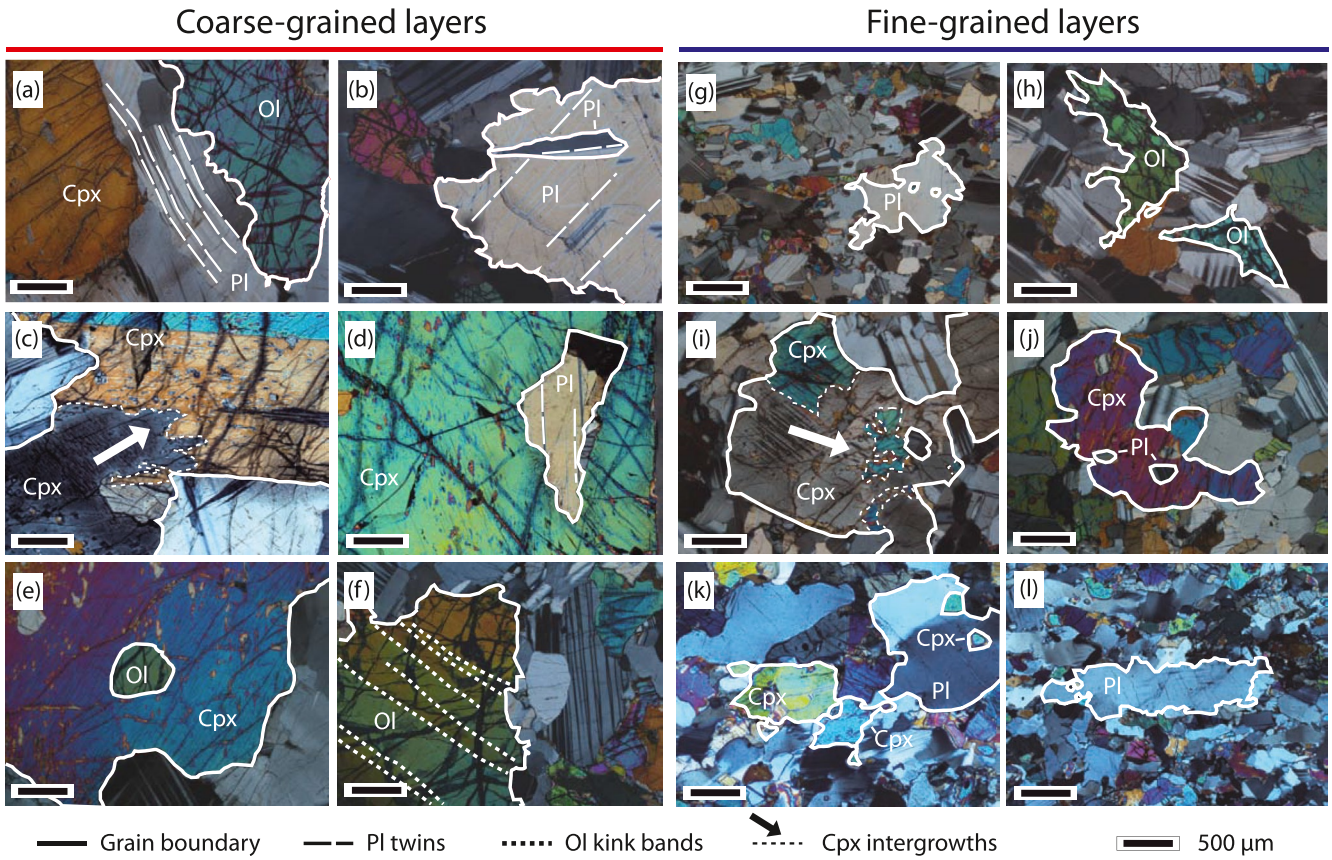


**Figure 3.** Photomicrographs in plane polarized light of characteristic textures identified in olivine gabbros from section 65R5. (a) Bent elongated Pl lath with well developed mechanical twins, and Ol with irregular and corroded grain boundary at the contact. (b) and (d) Small corroded Pl chadacrysts in Pl and Cpx. (c) Complex Cpx intergrowth, that is, Cpx with ragged grain boundaries and irregular interlocking Cpx grains. (e) Round-shaped Ol chadacryst within a larger Cpx. (f) Large Ol presenting well-developed kink bands. Cpx: clinopyroxene, Pl: plagioclase, Ol: olivine. Coarse-grained samples: (a) and (b) 65R5, 21–23 cm, (c) 65R5, 76.1–79.8 cm, (d) 65R5, 18.5–21.5, (e) 65R5-101.5–104, (f) 65R5, 99–101.5 cm. Fine-grained samples: (g) 65R5, 96–99 cm, (h), (i) and (j) 65R5, 39.5–43 cm, (j), (k) and (l) 65R5, 0–2.5 cm. See text for further descriptions.

round-shaped minerals (Figure 3e). Cpx are anhedral to slightly poikilitic, enclosing small Ol and mostly Pl chadacrysts (Figures 3d and 3e). Several crystals present complex Cpx intergrowths (ragged grain boundaries and irregular interlocking Cpx grains; Figure 3c) or brown amphibole blebs and associated secondary pyroxenes (Figures 3c–3e).

Fine-grained olivine gabbros present granular textures. Pl are subhedral to interstitial with magmatic twins and less developed tapered (mechanical) twins compared to the coarse-grained material. Some Pl minerals enclose very small Ol or Cpx chadacrysts (Figures 3g, 3k and 3l). Ol are present as small subhedral to anhedral grains with weak or no internal deformation (Figure 3h). Cpx are subhedral to interstitial, with the largest grains enclosing small—mostly—Pl chadacrysts (Figures 3i and 3j). Locally Pl and Cpx present clear resorbed grain boundaries or overgrowth at the expense of surrounding minerals (Figures 3h, 3k and 3l), and Cpx intergrowths also occur (Figure 3i). Two finer grained areas are observed within the studied section in the fine-grained layers, at ~4 cm from the top of the section at the contact with the overlying coarse-grained layer, and between ~85 and 90 cm from the top of the section in the form of 3 discontinuous stripes. On average the grain size of the finer grained bands is half the average grain size of the fine-grained layers. They appear in lighter gray on the whole round images of the section (stars in Figure 2b).

Out of the 8 subparallel contacts between fine- and coarse-grained layers, 5 are sharp and planar (at 2, 10, 25, 82 and 98 cm depth) and 3 are more diffuse (at about 43, 110, and 117 cm depth; Figure 2b). Sharp contacts are sutured, with interlocked fine- and coarse-grained minerals (Figure 2c). Locally at the contacts coarse Pl and Cpx show overgrowths toward the fine-grained material, enclosing small minerals (Figures 4d

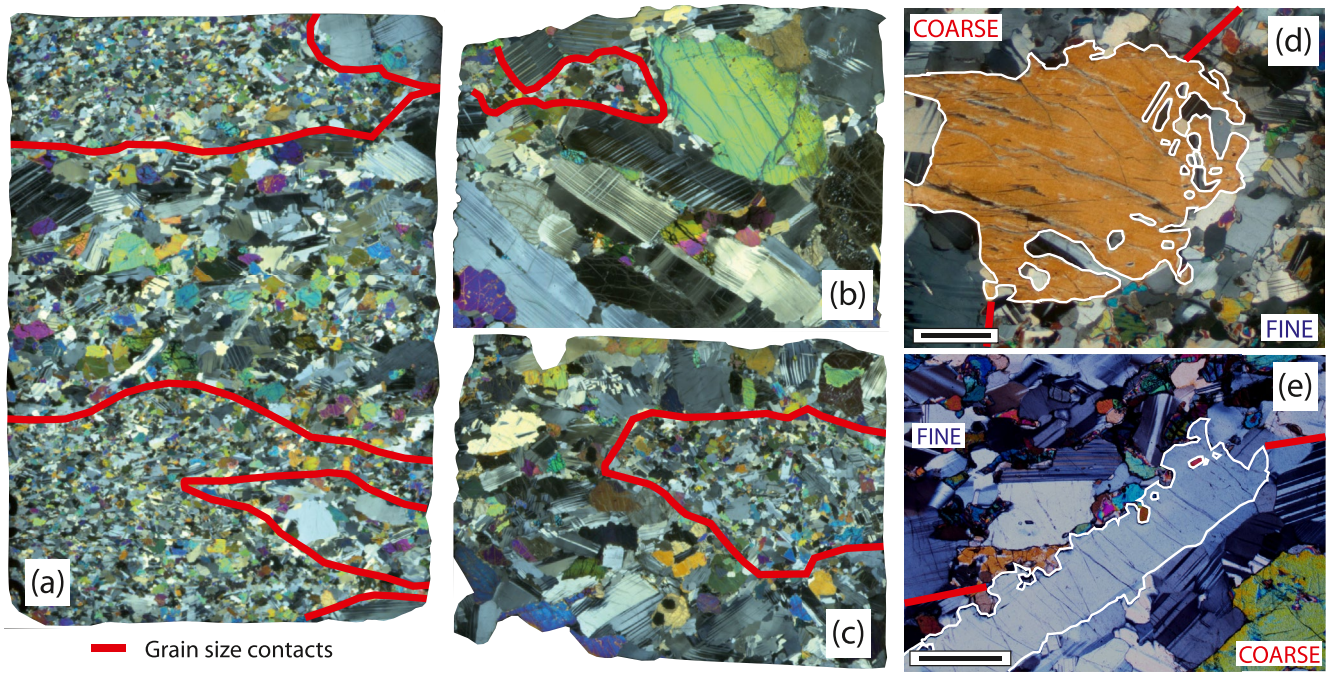


**Figure 4.** Details of thin sections scans (2 cm width) in plane polarized light for sample (a) 65R5, 83.5–87 cm showing enclaves of coarse-grained material in the fine-grained layer, and samples (b) 65R5, 12.5–15.5 cm and (c) 65R5, 21.5–23.5 cm showing fine-grained interstitial domains present in coarse-grained layers. (d) Cpx and (e) Pl at layer contacts presenting overgrowths toward the fine-grained material, enclosing small minerals (from sample 65R5, 79.5–83.5 cm and 65R5, 91–94 cm, respectively).

and 4e). At the thin section scale, both fine- and coarse-grained layers are heterogeneous, especially close to layer contacts. Fine-grained interstitial domains are present in the coarse-grained gabbros a few centimeters from the sharp contacts (Figures 4b and 4c), and conversely cm-wide lump or bands of coarse-grained material subparallel to the closest sharp contact are locally present in the fine-grained layers (e.g., at ~85 cm depth; Figure 4a). At diffuse contacts, we observe a progressive increase of the disseminated interstitial fine grains proportions in the coarse-grained material toward the fine-grained layers (Figure 2c). The mutual intrusion relations between fine- and coarse-grained materials will be discussed in the first section of Section 5 (in Section 5.1).

### 4.2. Microstructures

The average GOS (see Section 3.1) is 0.33° for Pl and 1.12° for Ol over the entire section, indicating that grains in fine- and coarse-grained layers are overall weakly deformed. In details, average GOS for fine-grained layers is 0.36° for Pl and 0.92° for Ol, and 0.30° for Pl and 1.34° for Ol for coarse-grained layers (Table S1). Cpx and Pl locally show minor recrystallization when present at contacts (Figure 5a). Although still weak, Pl grains are slightly more deformed in the finer grained bands of the fine-grained layers (average GOS of 0.54° for Pl in sample 65R5, 2.25–4 cm; Figure 5b).

Well-developed fabrics can be described in fine-grained layers, which strengthen toward contacts (see Table S1). These fabrics are parallel to the contacts between layers and are marked by a shape preferred orientation of Pl laths (see example in Figure 5d). CPO of Pl and Ol in the fine-grained layers have average $J$ of 2.5 and 2.6, respectively, and reach up to 3.34 for Pl next to the contact at ~80 cm from the top of the section (Table S1). Foliation is defined by the (010) planes of Pl, Ol, and Cpx, and lineations are marked by the (100) axis of Pl and the (001) axes of Ol and Cpx. For Pl, a BA-index close to 0 characterizes a perfect Axial-B fabric and translates the predominance of the foliation in the fabric (Satsukawa et al., 2013). For Ol, the predominance of the foliation is described by BC-indexes close to 0. The average BA of the fine-grained material is 0.38 for Pl and the average BC is also 0.38 for Ol. Similarly, the F# and L# parameters as defined by Cheadle and Gee (2017) characterize the relative strength of foliation (F#) and lineation (L#) described by Pl in

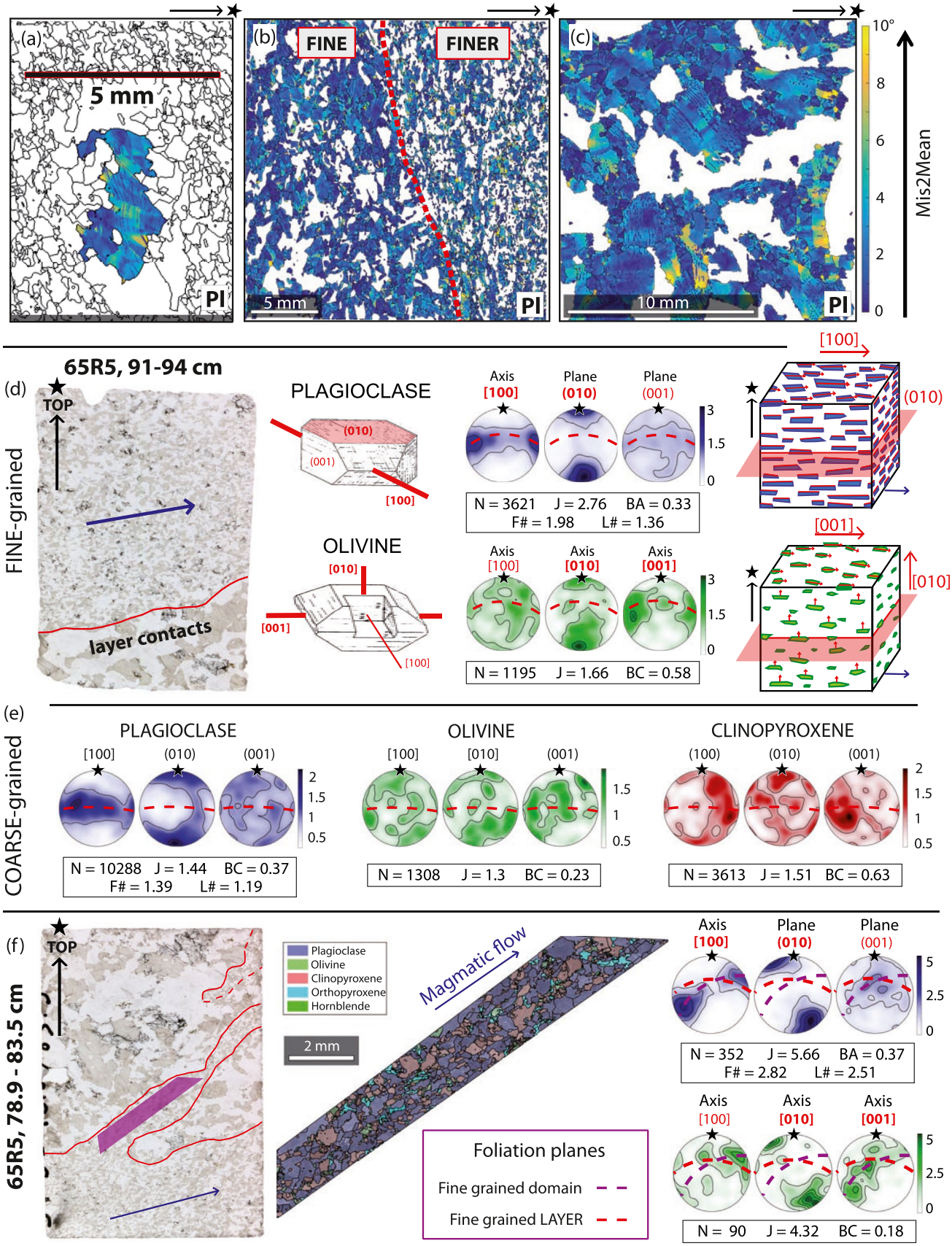
(a)
5 mm
Pl
(b)
FINE
FINER
5 mm
Pl
(c)
10 mm
Pl
10°
8
6
4
2
0
Mis2Mean
(d)
65R5, 91-94 cm
FINE-grained
TOP
layer contacts
PLAGIOCLASE
(010)
(001)
[100]
Axis [100]
Plane (010)
Plane (001)
3
1.5
0
N = 3621 J = 2.76 BA = 0.33
F# = 1.98 L# = 1.36
OLIVINE
[010]
[001]
[100]
Axis [100]
Axis [010]
Axis [001]
3
1.5
0
N = 1195 J = 1.66 BC = 0.58
[100]
(010)
[001]
[010]
(e)
COARSE-grained
PLAGIOCLASE
[100]
(010)
(001)
2
1.5
1
0.5
N = 10288 J = 1.44 BC = 0.37
F# = 1.39 L# = 1.19
OLIVINE
[100]
[010]
(001)
1.5
1
0.5
N = 1308 J = 1.3 BC = 0.23
CLINOPYROXENE
(100)
(010)
(001)
2
1.5
1
0.5
N = 3613 J = 1.51 BC = 0.63
(f)
65R5, 78.9 - 83.5 cm
TOP
Plagioclase
Olivine
Clinopyroxene
Orthopyroxene
Hornblende
2 mm
Magmatic flow
Foliation planes
Fine grained domain
Fine grained LAYER
Axis [100]
Plane (010)
Plane (001)
5
2.5
0
N = 352 J = 5.66 BA = 0.37
F# = 2.82 L# = 2.51
Axis [100]
Axis [010]
Axis [001]
5
2.5
0
N = 90 J = 4.32 BC = 0.18

**Figure 5.**

gabbroic samples. The average F# and L# of the fine-grained material are 1.88 and 1.35, respectively, and are consistent with other values for gabbros sampled at slow-spreading ridges (Table S1 and Figure S2; Cheadle & Gee, 2017; Ferrando, Basch, et al., 2021). One contact at ~80 cm from the top of the section is distinctly irregular, with the presence of a mm-thick portion of fine-grained material that crosscuts the coarse-grained layer at an angle of 30° to the contact (Figure 5f). This fine-grained domain has the same but stronger fabric compared to the rest of the fine-grained layer (*J* indexes of 5.66 and 4.32 respectively, BA index of 0.37 for Pl and BC index of 0.18 for Ol, F# of 2.82 and L# of 2.51 for Pl, Table S1). The fabric is also sub-parallel to the walls of the structure, as highlighted by the orientation of the foliation plane described Pl (100) planes for the fine-grained domain compared to the rest of the fine-grained layer (dashed lines, Figure 5f).

In contrast, no fabric can be identified in coarse-grained layers at the sample scale because the average grain size is too large relative to the core (~6 cm in diameter). At the scale of the section, the eight concatenated maps of coarse-grained layers (see Section 3.3) show a weak Pl CPO with a subhorizontal foliation (*J* index of 1.44 and BA index of 0.37, F# of 1.39 and L# of 1.19, Figures 5b and S2). No significant Ol or Cpx fabric is observed in those maps.

### 4.3. Whole Rock Compositions

The whole rock Mg# (molar ratio of $Mg/[Mg + Fe_{tot}] \times 100$) of the layers in section 65R5 ranges from 76.3 to 79.3 mol%, whereas the Ca# (molar ratio of $Ca/[Ca + Na] \times 100$) varies slightly between 72.3 and 74.7 mol% (Figure 6a). When compared with whole-rock major and minor element compositions in ODP Hole 735B (Dick et al., 2000) and of other samples from U1473A (MacLeod et al., 2017b), our data fall within the compositional range of Atlantis Bank olivine gabbros (Mg# between 62 and 84 mol% and Ca# between 56 and 83 mol%). The studied samples are nevertheless more primitive than the average bulk composition of the three ODP-IODP Holes drilled at Atlantis Bank (average respective Mg# and Ca# of 71 mol% and 69.7 mol% for IODP Hole U1473A, 73 mol% and 70.3 mol% for ODP Hole 735B, and 53 mol% and 65.6 mol% for ODP Hole 1105A; MacLeod et al., 2017a).

The trace element compositions of the fine- and coarse-grained layers are very similar, and span a relatively narrow range compared to the variability observed in olivine gabbros from holes 735B or U1473A (Figures 6b and 6c). They present strong positive Sr and Eu anomalies and their rare earth element (REE) contents vary within the range of olivine gabbros from ODP Hole 735B (Figure 6c). The REE compositions of coarse- and fine-grained layers are depleted relative to primitive mid-ocean ridge basalt (MORB), with the most incompatible elements (light REEs) being the most depleted (average $La_N/Sm_N$ of 0.62). In summary, fine-grained layers have higher Mg# and compatible elements contents (e.g., Cr), and are depleted in incompatible elements (e.g., Y and REE) compared to the coarse-grained layers (see Figure 6 and Table S2 for details).

### 4.4. Mineral Major and Minor Element Compositions

Pl compositions are homogeneous along the studied section (Figure 7a). The majority of the anorthite (An) contents of Pl (molar $Ca/[Ca + Na + K] \times 100$) ranges from 57.3 to 62.6 mol% in the fine-grained layers and

**Figure 5.** Grain misorientation maps describing the deformation of Pl grains and characteristic sample fabrics identified in section U1473A-65R5. (a) A single coarse-grained Pl crystal located at a lithological contact at ~80 cm depth. Deformed Pl twins are visible. (b) A fine-grained lithology that transitions to a finer grained band to the right at ~3 cm depth. The average grain orientation spread (GOS) for the fine-grained area to the left is 0.32° and is 0.54° for the finer-grained lithology to the right. (c) A coarse-grained lithology at ~76 cm depth. The average GOS in this area is 0.37°. White areas: other minerals. (d) From left to right: thin section scan of the contact between fine-grained (top) and coarse-grained (bottom) lithologies at ~91 cm depth (~2 cm width); crystallographic characteristics of Pl and Ol crystals (red lines, crystallographic axes; red surfaces, crystallographic planes); Pl and Ol crystal preferred orientations (CPOs) analyzed in the fine-grained material (red dashed lines, orientation of the foliation plane as defined by Pl (100) preferred orientation; *N*, number of grains considered); and 3D schematic diagrams representing the orientation of Pl and Ol crystals (and their crystallographic characteristics) within a magmatic flow as described by the blue arrows. (e) CPOs of Pl, Ol, and Cpx analyzed in the concatenated maps of the coarse-grained samples. (f) From left to right: thin section scans of a contact between fine- (bottom) and coarse-grained (top) lithologies (purple area, surface analyzed separately to obtain CPOs within the incursion of fine-grained material, ~2 cm width); mineralogical map corresponding to the purple area; Pl and Ol CPOs (purple dashed lines, orientation of the foliation plane as described by pl (100) planes, compared with the foliation plane described by Pl in the rest of the fine-grained layer below the contact in red dashed lines). The black arrows and stars indicate the direction to the top of the section.

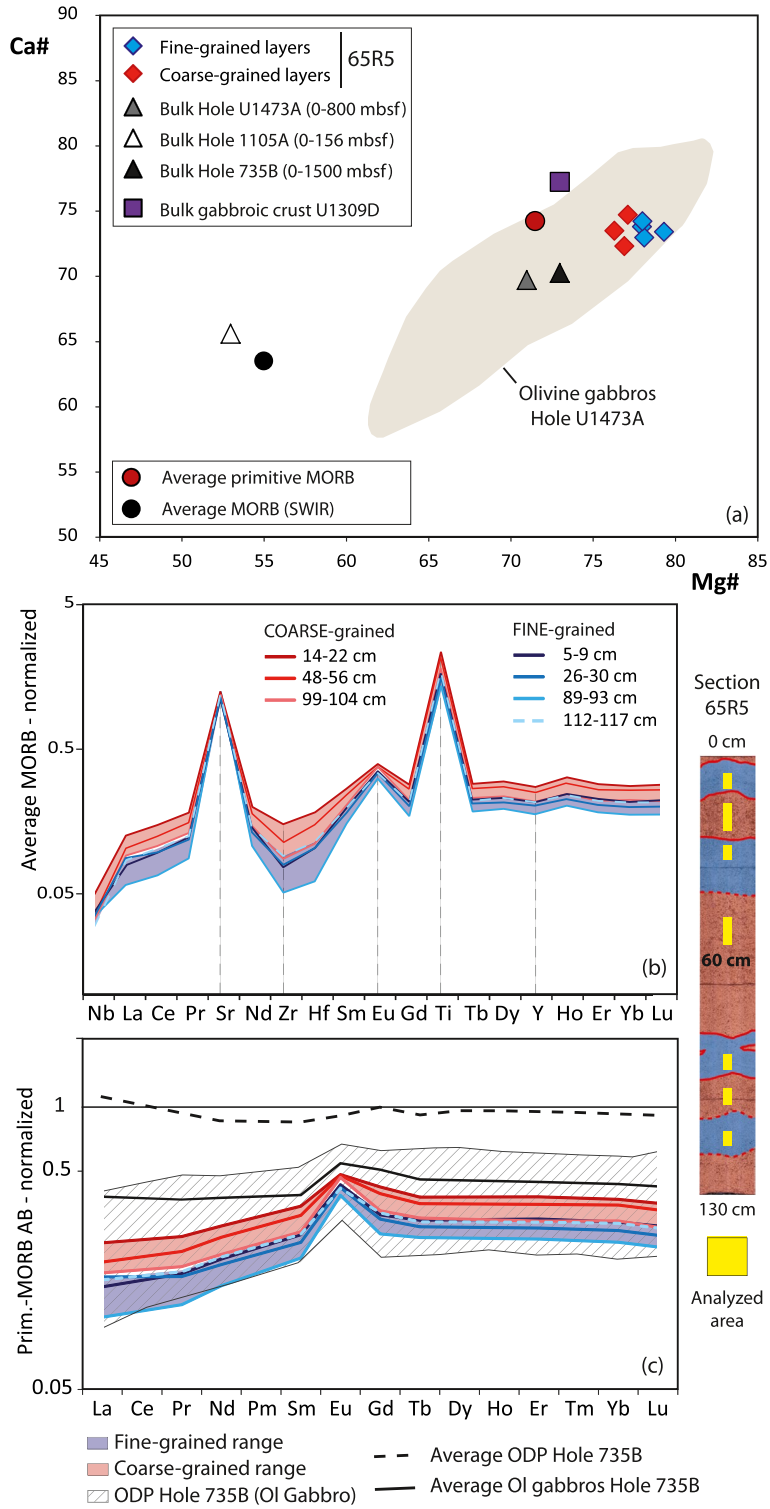


**Figure 6.**

from 53.4 to 64.5 mol% in the coarse-grained layers. Minerals of the localized fine-grained domains located within the coarse-grained layers, and of the coarse-grained lumps located within the fine-grained layers present the same An ranges (56.2–62 and 56.4–65.7, respectively), which are similar to the An values recorded in ODP Hole 735B olivine gabbros (Dick et al., 2002). Some Pl (~4% of the analyzes) display very thin

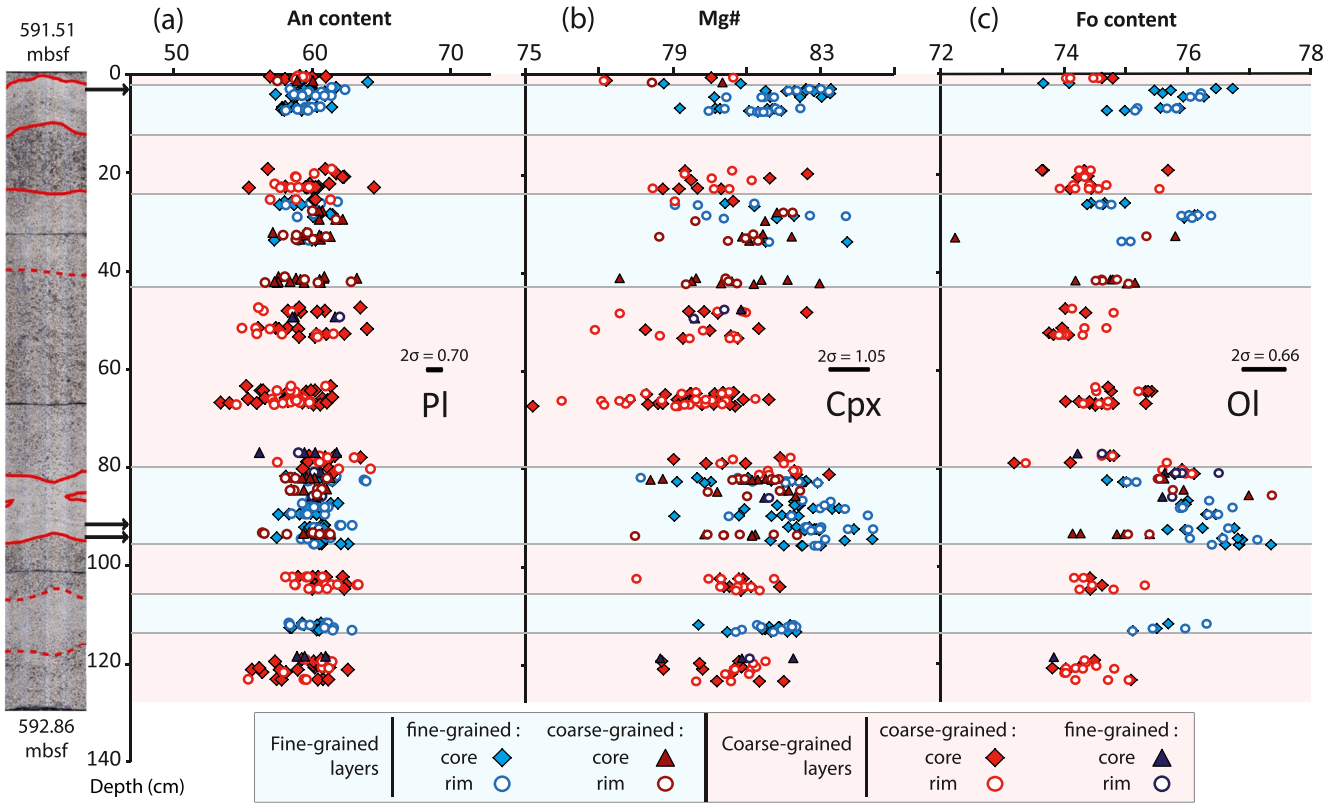


**Figure 7.** Depth profiles (cm from the top of the section) of (a) Pl An contents, (b) Cpx Mg#, and (c) Ol Fo content, in mol%. Blue points represent analyses of fine-grained materials, red points of coarse-grained materials. Reported errors correspond to propagated 2$\sigma$ errors on the considered elements. Black arrows represent the approximate location of the finer grained areas of the fine-grained layers. Left: whole round image of section 65R5 with associated layer contacts (see Figure 2).

(<10 μm wide) outer discontinuous rims enriched in An contents (up to 75.8) than in Pl cores and rims (as low as 58.9), mostly in the fine-grained layers. Beyond this local observation, no clear core-rim zoning feature has been observed in the studied section (Figure 7a). Such very localized An enrichments close to grain boundaries has been reported in Boulanger et al. (2020), and are very similar to those observed by Koepke et al. (2005) in various localities at fast- and slow-spreading ridges. Those authors interpreted those features as a consequence of hydrous anatexis within the crust. In addition to the fact that these rims are scarce in the studied section, their study is beyond the scope of this study, and will not be discussed in further details (corresponding data are presented in Table S3 and named as "outer rim").

Cpx Mg# presents more variability with depth than the Pl An contents. The values are slightly higher in the fine-grained (78.1–84.4 mol%) than in the coarse-grained Cpx (75.2–83.2 mol%, Figure 7b). Minerals from the fine-grained domains located within the coarse-grained layers, and from the coarse-grained lumps located within the fine-grained layers present similar values (78.7–82.3 mol% and 77.6–83 mol%, respectively). Cpx $TiO_2$ and $Cr_2O_3$ contents are rather homogeneous with varying depth (0.39–1.34 wt% $TiO_2$ and 0–0.24 wt% $Cr_2O_3$; Table S3). These compositions fall within the range covered by Cpx from ODP Hole 735B

**Figure 6.** Whole-rock (a) Ca# and Mg# of olivine gabbros from each layer of section U1473A-65R5, and comparison with other olivine gabbros from Hole U1473A, Atlantis Bank bulk holes U1473A, 735B, and 1105A, and Atlantis Bank bulk hole U1309D (from MacLeod et al., 2017a), average mid-ocean ridge basalt (MORB) compositions from the same authors. (b) Spider diagram normalized to an average MORB composition (Gale et al., 2013) and (c) Rare earth element profiles normalized to the average of the most primitive MORBs sampled on the Atlantis Bank section of the SWIR (Table S5; from Coogan et al., 2004) for each layer sampled in section U1473A-65R5. Red and blue shaded areas correspond to fine- and coarse-grained olivine gabbros, respectively. The hatched domain in panel (c) corresponds to the compositional range of olivine gabbros from ODP Hole 735B (Dick, Meyer, et al., 1991; Dick et al., 1999; Hart et al., 1999; Hertogen et al., 2002; Holm, 2002; Shipboard Scientific Party, 1989), with the solid black line representing the average composition of olivine gabbros and the dashed black line the average composition of the entire ODP Hole 735B.

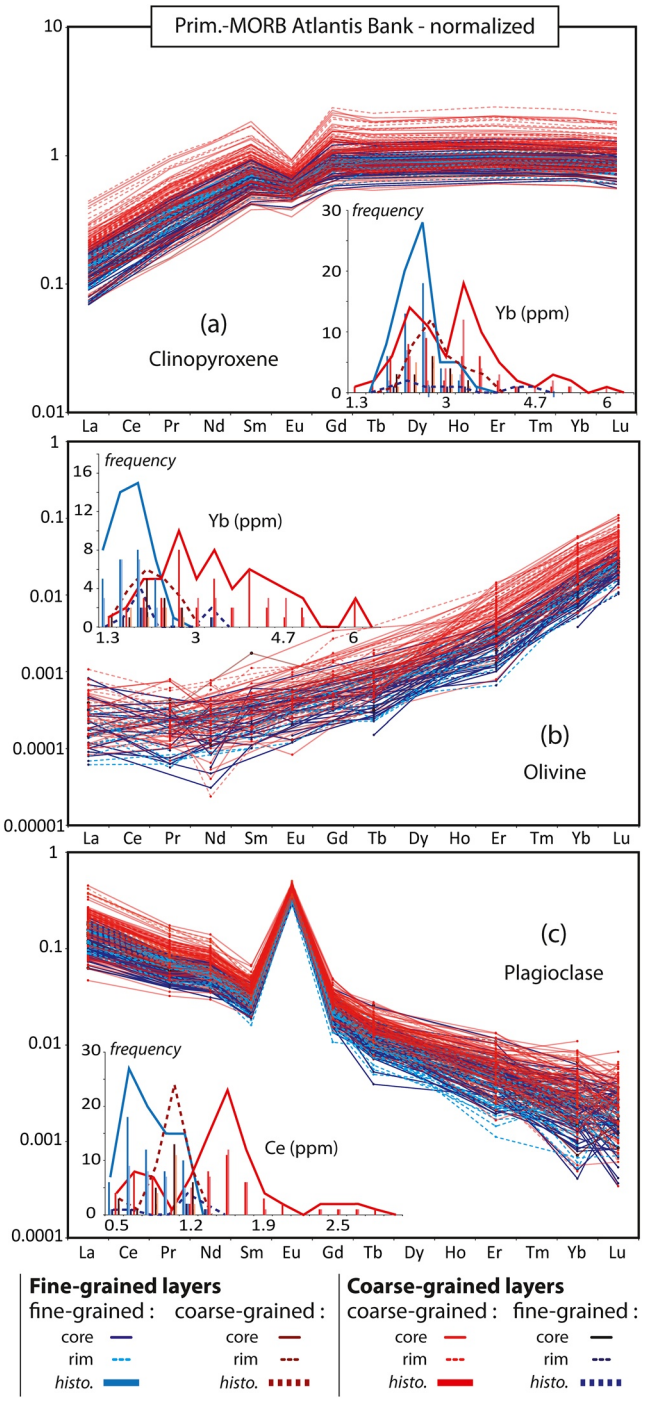


**Figure 8.** Rare earth element (REE) normalized to the average of the most primitive mid-ocean ridge basalt sampled on the Atlantis Bank section of the SWIR (from Coogan et al., 2004; Table S5) concentration diagrams for (a) Cpx, (b) Ol, and (c) Pl from section 65R5. Solid and dashed lines indicate crystal cores and rims, respectively. Histograms indicate the compositional distribution of the most abundant REE analyzed in Pl and Ol, and that of the most fractionated REE in Cpx. The frequencies represent the total number of analyses for each lithology, which are lower for the fine-grained compared to the coarse-grained layers (by 40 for Pl and Cpx, and 30 for Ol).

olivine gabbros (Dick et al., 2002). Notably, no systematic chemical zoning of Cpx crystals is observed in the fine-grained or in the coarse-grained layers.

Ol forsterite (Fo) contents are homogeneous in a given sample, and are generally higher in the fine-grained layers (73.7–77.4 mol%) than in the coarse-grained layers (73.2–76.1 mol%), although the ranges are similar (Figure 7c). Notably, Ol from the coarse-grained lumps within fine-grained layers seem to locally preserve low Fo contents (e.g., at ~93 cm depth, coarse-grained Ol Fo of 74.1–75.4 mol%, and fine-grained Ol Fo of 75.7–76.7 mol%). Contrastingly, the NiO and MnO contents of Ol are homogeneous throughout the section in both the fine- and coarse-grained layers (0–0.15 wt% NiO and 0.24–0.45 wt% MnO), and fall within the Ol range from ODP Hole 735B olivine gabbros (Dick et al., 2002). No systematic core-to-rim variation is observed.

Overall, mineral major and minor element compositions display small variations throughout the studied section (Figure 7, Table S3), and no systematic compositional zoning is present.

### 4.5. Mineral Trace Element Compositions

Mineral-specific REE contents are on average higher and are more variable in coarse- than in fine-grained layers (Figures 8 and 9). For example, the average Cpx Ce content in fine-grained layers is 1.87 ± 0.46 ppm, and 2.96 ± 1.17 ppm in the coarse-grained layers. In a single coarse-grained sample located at ~20 cm below the top of the studied section, Cpx Ce contents vary by a factor of ~6 (i.e., from 1.15 to 6.45 ppm, Figure 9b). This variability is also described by the histograms of the most abundant REE compositional distribution presented in Figure 8a. The frequency peaks for fine-grained layers are focused on lower REE values than the equivalent peaks for coarse-grained layers (i.e., there is less compositional variation in fine-grained layers). In contrast, the values for coarse-grained samples are more dispersed and span the entire range of composition of the fine-grained layers, in addition to showing the highest contents analyzed in the studied section (also as observed in the spider diagrams of Figure 8).

In addition to the difference between fine- and coarse-grained materials, the compositions of coarse- and fine-grained layers taken separately are not homogeneous throughout the section. The central sample of the coarse-grained layer (from 42 to 80 cm from top) that is located at ~63 cm from the top of the section stands out of the general pattern described above. The minimum compositional values of that layer (e.g., 2.49 ppm Ce in Cpx and 0.45 ppm La in Pl) are higher than in any other coarse-grained layer of the studied section (0.94 ppm Ce in Cpx and 0.13 ppm La in Pl; Figure 9). Closer to the contacts between layers, the coarse-grained material shows trace element contents similar to those analyzed in the adjacent fine-grained layers (compositional ranges of Figure 9). The finer grained bands located within the fine-grained layers described in Section 4.1 also present distinctive trace element signatures compared to the rest of the fine-grained layers. Cpx of those finer grained bands present depletion in light REE compared to heavy REE, resulting in La/Lu ratios normalized to a primitive MORB lower than ~0.6 and reaching values lower than 0.3 (at ~92 cm depth, Figure 10). In general, the ratios of more to less incompatible trace elements in Cpx vary with depth, and within

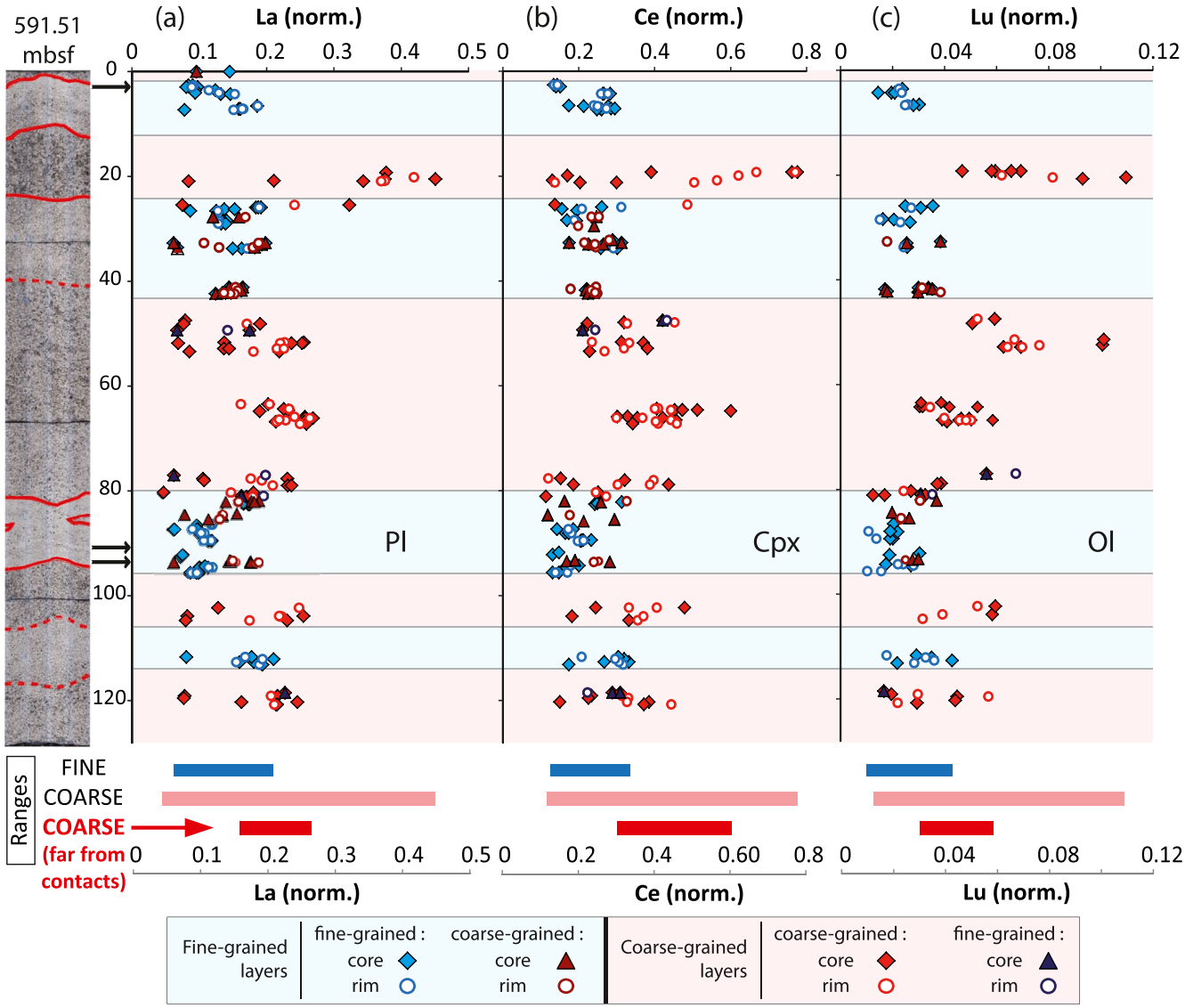


**Figure 9.** Depth profiles (cm from the top of the section) of (a) La in Pl, (b) Ce in Cpx, and (c) Lu in Ol, normalized to the average primitive mid-ocean ridge basalt of the Atlantis Bank area (Table S5). The compositional ranges of each lithology throughout the section are represented by the colored boxes at the bottom of the figure. The compositional range describing the coarse-grained lithology far from any lithological contacts (darker red) corresponds to the two samples from ~63 cm depth. Black arrows represent the approximate location of the finer grained areas of the fine-grained layers. Left: whole round image of section 65R5 with associated layer contacts (see Figure 2).

each layer. The average $La_N/Lu_N$ ratio is lower in fine- than in coarse-grained layers (0.76 and 0.97, respectively). The minimum $La_N/Lu_N$ value of the central coarse-grained layer at ~63 cm below the top of the studied section is again higher than the minimum ratios observed elsewhere in the section (0.75 compared to 0.59, respectively; see Figure S3 for more details).

## 5. Discussion

Thanks to the new results presented herein, we aim at identifying the signification of localized igneous layers in slow-spreading lower oceanic crust, and potentially improving our knowledge of igneous accretion at those locations. In the following, we first discuss the implications of the petro-structural data in terms of chronology of emplacement of the fine- and coarse-grained layers (Section 5.1), before discussing chemical data to tackle the differences between the magmas that formed those layers, and the interactions that

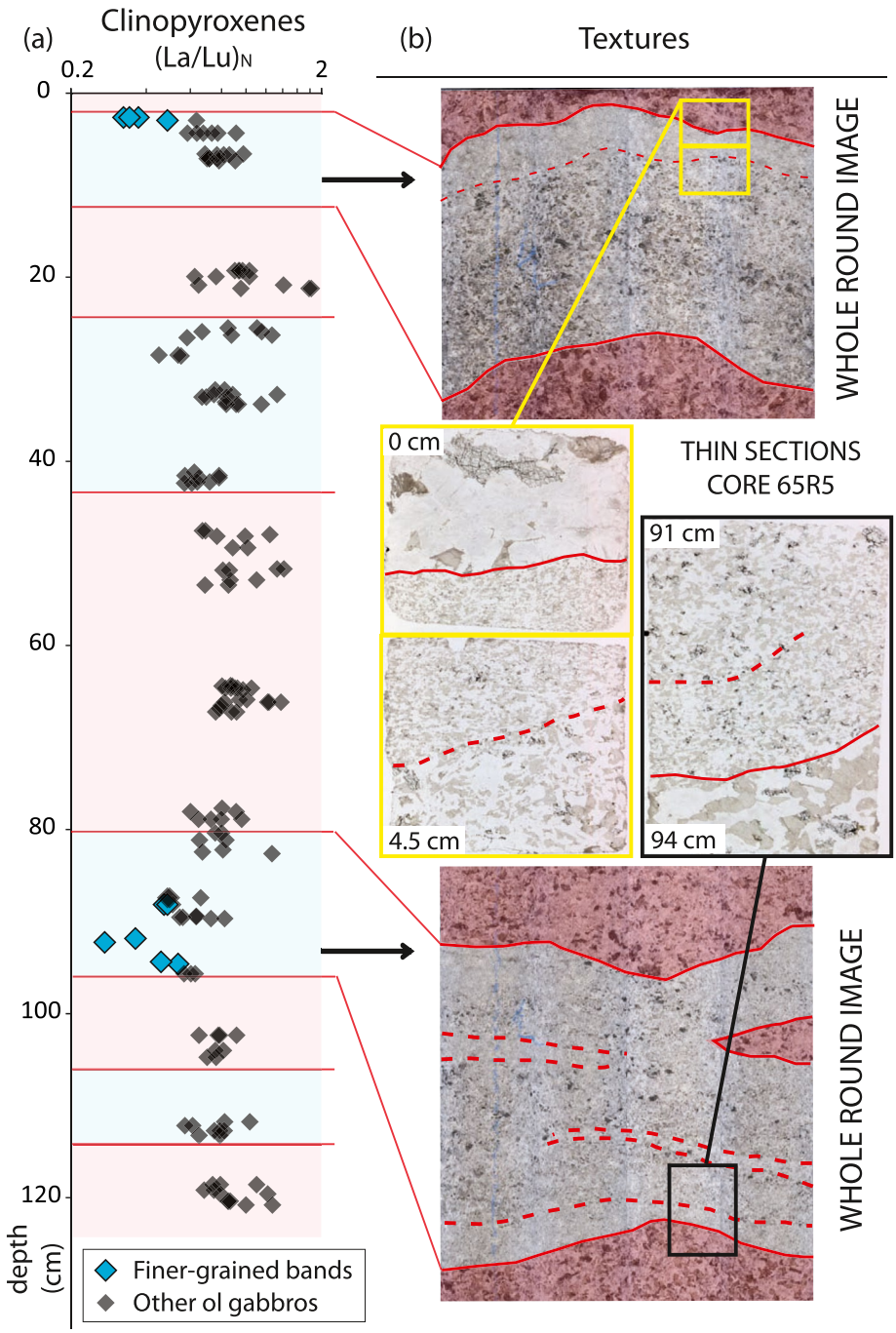


**Figure 10.** (a) La/Lu ratio of Cpx analyzed in the coarse- and fine-grained layers, normalized to the average primitive mid-ocean ridge basalt composition of the Atlantis Bank area (Table S5). Analyses from the finer grained bands of the fine-grained layers are represented in blue. Red lines: layer contacts. (b) Textural details of the two zones presenting finer grained bands. Top and bottom: whole round scans (contacts between finer grained material and the surrounding lithology represented by red dashed lines). Center: photomicrographs of the corresponding thin sections (~2 cm width). Areas in red correspond to the coarse-grained layers.

occurred at their contacts (Section 5.2). We then discuss the evolution of the mushy system in both types of layers (Section 5.3) before proposing an emplacement model as part of magma reservoirs formation and evolution at slow-spreading centers.

### 5.1. Origin of the Sparse Layering at a Slow-Spreading Center

In order to determine the origin of the layering described herein, we first have to determine the respective implication of both solid-state deformation and magmatic processes in their formation. Microscopic observations and EBSD data enable us to discard crystal-plastic deformation being responsible for the formation of the fine-grained lithology from an initial coarse-grained one. Strong evidences of crystal-plastic deformation such as extensive recrystallization or intra-grain deformation are almost absent in both lithologies, and internal deformation as determined by EBSD is low (average GOS is 0.30 for Pl, Figures 5b and 5c). The Pl fabric of both fine- and coarse-grained layers is a classical axial-B CPO (average BA indexes of 0.38 and 0.37 for Pl, respectively, Figure 5e). This CPO is characteristic of magmatic fabrics formed for example by crystal alignment during magmatic flow or crystal settling (Jousselin et al., 2012; Morales et al., 2011; Satsukawa et al., 2013). In fine-grained layers, Ol CPO (Figure 5d) with respect to the reference frame defined by the Pl grains is consistent with crystal alignment during magmatic flow. In coarse-grained lithologies only Pl attests to a magmatic fabric. No fabric was detected for Ol or Cpx even after merging the EBSD maps to get better statistics (Figure 5e). In addition to these magmatic fabrics, the granular to subophitic textures of the olivine gabbros further confirm the magmatic origin of both coarse- and fine-grained layers.

Several processes can account for the formation of igneous layers (e.g., crystal settling or density currents, variations in nucleation or growth rates, compaction waves..., see summary in Namur et al., 2015). Here, clear local intrusive relation of the fine-grained material in the coarse-grained layers, represented by the small fine-grained domain crosscutting the coarse-grained material (Figure 5f), strongly supports a model in which one magma intrudes a partially to totally crystallized medium. The intrusive character of the fine-grained lithology is also supported by the increase in foliation and lineation intensities toward the layers boundaries. The orientation of the fabrics is constrained by the geometry of the layer boundaries, such as in the small intrusive domain highlighted in Figure 5f, where the foliation slightly rotates to stay parallel to the intrusive contacts. Our results support that fabric in fine-grained layers is controlled by the geometry of the contacts due to orientation of the crystals in the flowing magma. In this perspective, coarse-grained domains in fine-grained layers represent enclaves of the intruded medium (see Figure 4a). The mushy character of the intruded coarse-grained material is supported by the presence of sutured contacts between the layers, by intermixed fine- and coarse-grained material at diffuse contacts (Figures 2 and 4), and by the absence of truncated crystals at the margins of the coarse-grained layers. In addition, the Pl CPO of the fine- and coarse-grained lithologies are sub-parallel, and little intra-grain deformation is present. This can potentially be explained by moderate compaction of the layers in the same strain field and in the presence of melt, attested by the presence of weak intra-grain deformation features (see Section 4.1, Ferrando, Basch, et al., 2021), thus allowing movement of the crystals without breaking them and the superimposition of a similar fabric in both lithologies. Overall, the formation model that best accounts for the various textural and structural characteristics described herein is by intrusion of a magma that will form the fine-grained material, into a coarse-grained mushy domain. Both potentially suffered slight compaction later on, aiding interstitial melt extraction.

### 5.2. Constraints on the Parental Magmas and Interactions Between Layers

#### 5.2.1. Comparison Between Fine- and Coarse-Grained Lithologies

Whole-rock incompatible element contents show that both coarse- and fine-grained layers have a cumulative signature (positive Sr and Eu anomalies, and depletion in incompatible elements relative to primitive MORB; Figure 6b). It is therefore clear that fine-grained gabbros do not represent frozen melts as previously proposed for some microgabbros at Atlantis Bank (Dick, Kvassnes, et al., 2019; Dick, Meyer, et al., 1991). In addition, coarse-grained layers are more enriched in incompatible elements than fine-grained layers (Figures 6b and 6c), suggesting that the coarse-grained lithology either formed from a more evolved melt, differentiated to greater extents, or contain more trapped interstitial melt than fine-grained layers.

In order to discuss the composition of the parental melts of both fine- and coarse-grained layers, we hereafter use the most depleted values of a given sample. Indeed the most depleted values, of both fine- and coarse-grained layers, are of particular interest as they constrain the composition of the most primitive magma from which the minerals crystallized. Also to avoid any geochemical modification due to interactions between layers (see later Sections 5.2.2 and 5.3.4), we first only compare *in situ* mineral chemical compositions of the fine-grained material with those measured in the central part of the thickest coarse-grained layer (i.e., the farthest from any contact; coarse-grained sample from ~63 cm below the top of the section). A key difference between the two layer types is that the lowest incompatible element contents, especially REE in Ol, Pl, and Cpx, are notably higher in coarse-grained samples of the central coarse-grained layer compared to the fine-grained counterpart (Figure 9). This suggests that both layers crystallized from parental magmas that were chemically distinct (either from different sources or at different stages of evolution).

In general, compared to the coarse-grained layers, the fine-grained lithology displays no strong variability or enrichments in REE in minerals with a maximum variation factor of 1.9 for Ce in Cpx (in coarse-grained material, the highest Ce contents are up to 5.6 times the lowest ones for a given sample). This difference could have been related to an analytical bias due to the large laser ablation spot size compared to the size of the minerals analyzed in the fine-grained layers. To test this hypothesis, we estimated the compositional impact if only a small fraction of an enriched rim (with a similar enrichment as that in the coarse-grained material) was included in an analysis of a grain with a core composition equivalent to the less differentiated compositions of our fine-grained samples (details in Text S3). The results show that less than 25% of the volume analyzed needs to comprise such hypothetical enriched rims to produce the upper bound of the fine-grained samples compositional range. If such enriched rims were present, given the number of measurements conducted, we should have detected them in our samples. Hence, the lack of high incompatible elements enrichments from crystal core to crystal rim in fine-grained material is a primary feature. More importantly, fine-grained Cpx present stronger fractionations between light and heavy REEs with lower $La_N/Lu_N$ values ($La_N/Lu_N$ = 0.07–0.20) compared to Cpx in the coarse-grained lithology ($La_N/Lu_N$ = 0.09–0.28) that cannot be explained by an analytical bias. Our results eventually highlight that coarse- and fine-grained materials crystallized from distinct parental melts, with the coarse-grained one being more enriched, and the fine-grained one displaying a lower La/Lu ratio.

#### 5.2.2. Consequences of the Intrusive Event and Interactions Between Layers

As presented above, the coarse-grained layers are chemically heterogeneous throughout the section. Notably, the minimum incompatible element contents observed in coarse-grained minerals near the boundaries of coarse-grained layers are similar to those of the neighboring fine-grained layers, whereas the lowest contents in the central part of the thickest coarse-grained layer (~40–80 cm from the top of the section), away from the contacts, are higher (at ~63 cm from the top of the section; see ranges in Figure 9). Similarly, the small enclaves of coarse-grained material present in the fine-grained layers often display depleted signatures similar to those observed in minerals from fine-grained layers (e.g., at ~33 cm depth; Figure 9).

Macro-scale diffusion between layers during subsolidus re-equilibration could explain these depleted signatures in coarse-grained layers along the contacts with fine-grained ones. However, no combined increase in incompatible trace element contents are recorded near the contacts in fine-grained lithology indicating that the implication of such a macro-scale diffusion process in the studied samples is unlikely. In addition to this compositional variation across contacts, diffusion reequilibration is unlikely as inter and intragrain heterogeneous compositions of minerals are widespread (Figures 7 and 9). For example, the Fo contents of Ol from a coarse-grained enclave at ~93 cm from the top of the section are clearly distinct from the Ol compositions of the enclosing fine-grained material (Figure 7c). Thus, we do not observe cm-scale diffusion profiles across contacts between the lithologies, even though Fe and Mg are fast-diffusing elements in Ol. As other major and trace elements considered herein diffuse more slowly in Pl or Cpx, cm-scale diffusion cannot explain the geochemical variations observed in coarse-grained layers near lithological contacts.

If not diffusion, the best explanation for the compositional changes of coarse-grained layers near contacts is the occurrence of interactions at the time of the intrusion, between the mushy coarse-grained material and the infiltrating parental magma of the fine-grained lithology. This hypothesis is supported by the heterogeneous textures of the coarse-grained material near contacts, with either interstitial fine-grained domains near sharp contacts (Figures 4b and 4c), or the progressive transition from coarse-to fine-grained material

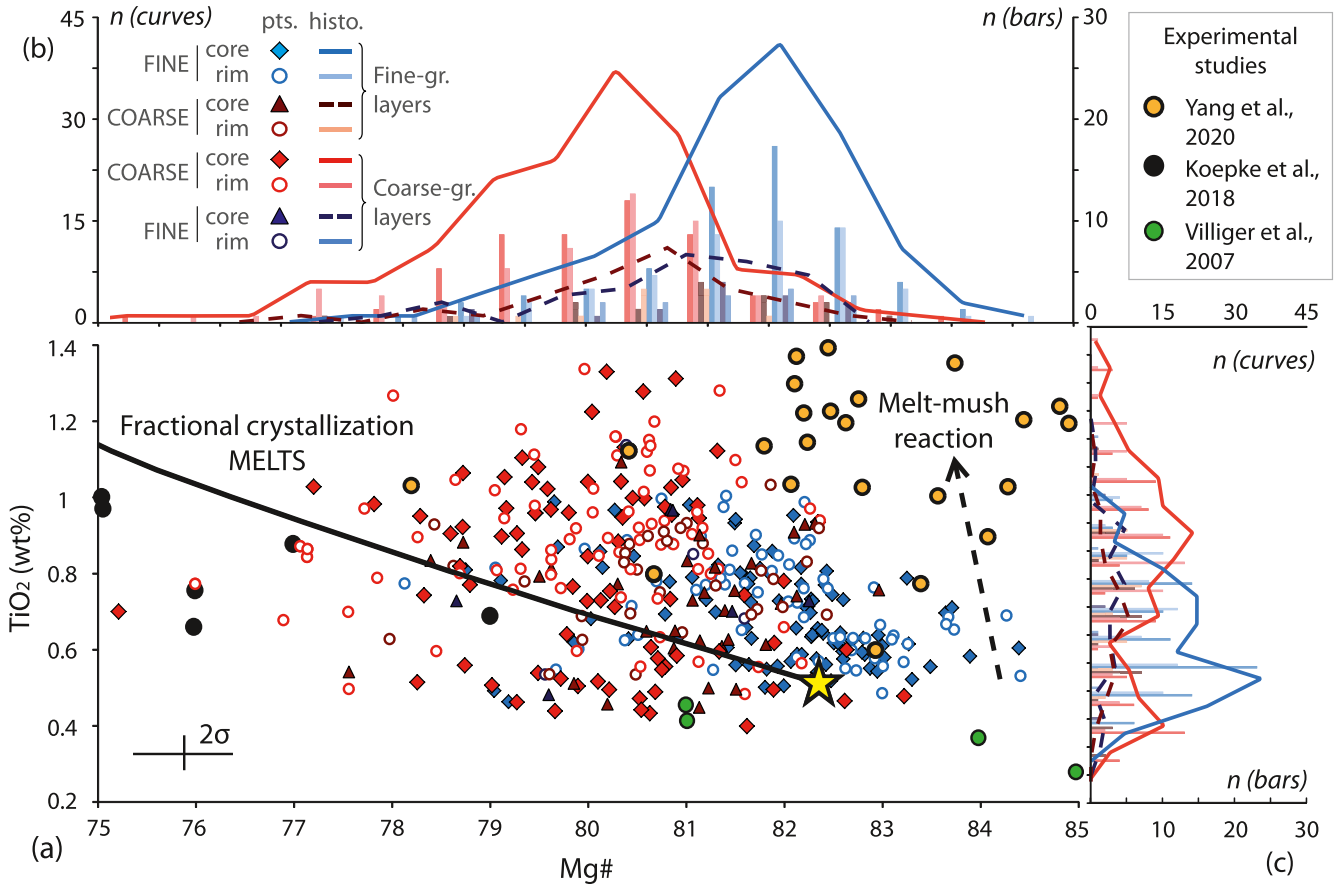


**Figure 11.** (a) $TiO_2$ (wt%) versus Mg# (mol%) of Cpx from section 65R5 and corresponding (b) histograms for Mg# and (c) $TiO_2$ content of the analyzed grains. The fractional crystallization trend represents crystallization of the average primitive MORB value by MELTS (yellow star, Table S6). Results of equilibrium crystallization experiments on late-stage MORBs from Koepke et al. (2018), results of equilibrium and fractional crystallization experiments on a tholeiitic magma from Villiger, Ulmer, and Müntener (2007), and interaction experiments between a troctolite cumulate equivalent and MORBs from Yang et al. (2019) are reported for comparison.

at diffuse contacts (Figure 2c). The center of the thickest coarse-grained layer (~63 cm from the top of the section, Figure 9) seems unaffected, suggesting that permeability was limited in the coarse-grained material at the time of intrusion as the intruding magma was unable to migrate at ~20 cm within the layers (distance to the center of the thickest coarse-grained layer). The interaction process at the layers contacts will be quantitatively modeled in the next Section 5.3.4.

### 5.3. Magmatic Evolution of the Layers

The parental melts that formed fine- and coarse-grained layers likely underwent various magmatic processes after emplacement, which may include crystallization (equilibrium or fractional), and postcumulus processes such as RPF or trapped melt crystallization. In the following, we focus on deciphering the processes that led to the formation of both layer types based on sample textures and chemical data to eventually identify the different steps of formation of the layered section.

#### 5.3.1. Evolution of the Coarse-Grained Layers Prior to Fine-Grained Material Intrusion

In coarse-grained layers, the $TiO_2$ contents of Cpx are higher at a given Mg# than expected after magmatic crystallization only of a primitive MORB magma from the Atlantis Bank area (Figure 11; MELTS model detailed in Text S4 and Table S6). Equilibrium and fractional crystallization of typical tholeiitic melts determined experimentally produce Cpx with $TiO_2$ contents lower than 0.6 wt% (Villiger, Ulmer, & Müntener, 2007; Figure 11). Even Cpx crystallization from late-stage Ti-rich MORB-type melts produces

Cpx with lower $TiO_2$ contents at a given Mg# that in the Cpx from the studied series (Koepke et al., 2018). Ross and Elthon (1997) described similar anomalous $TiO_2$ Cpx contents in oceanic olivine gabbro samples from the Mid-Atlantic Ridge, and argued for the occurrence of "postcumulus crystal growth from, or interaction with evolving intercumulus melts" to explain such Ti over-enrichments. The favored model of Ross and Elthon (1997) is the occurrence of trapped melt crystallization and late magmatic reequilibration, which is classically considered for the evolution of igneous cumulates (e.g., Bédard, 2015; Borghini & Rampone, 2007; Coogan et al., 2000). Beyond trapped melts, a RPF process can alternatively explain Cpx Ti over-enrichments. Indeed, experiments reproducing RPF processes and the interactions between a dunitic analog and MORB-type glasses by Borghini et al. (2018) led to crystallization of Cpx with high Mg# together with very high $TiO_2$ contents. Yang et al. (2019) obtained similar results by interaction of a troctolite equivalent with different MORB-type melts that were initially not particularly enriched in Ti, and which led to the formation of Cpx with similar $TiO_2$ contents at a given Mg# compared to our samples (Figure 11). Hence, crystal-melt interactions and RPF are also potentially involved in the formation of the coarse-grained lithologies.

The implication of crystal-melt interactions and RPF is also supported by considering the Cpx trace element contents. REE concentrations vary greatly at the scale of a single thin section, with variations reaching a factor of 6 for Cpx Ce contents at ~20 cm below the top of the section (ratio between the lowest and the highest trace element contents in a single sample—Figure 9). If we exclude areas affected by contact interactions and consider only the value recorded in the central coarse-grained layer, the variation factors are lower (e.g., 2.34 for Cpx Ce contents). To test whether those geochemical signatures from the central coarse-grained layer can be reproduced by a fractional crystallization process, we modeled the evolution of an equivalent primitive melt from the Atlantis Bank area following the method developed in the supplementary materials (see Text S4). The results show that a Ce enrichment factor of about 2.3 is attained after 60% fractional crystallization. Such extensive crystallization seems unlikely considering the major element compositions of the analyzed minerals; the expected Cpx Mg# obtained by using MELTS thermodynamic model (Text S4) after 60% fractional crystallization is 73 mol%, whereas the lowest observed value (in the sample at ~20 cm depth) is 79 mol%. In addition, the expected fractionations between more and less incompatible REEs ($La_N/Lu_N = 0.19$ at 60% fractional crystallization) are lower than most of the range observed in our samples ($La_N/Lu_N = 0.18–0.21$, Figure 12b). We also tested the effect of temperature variations during crystallization on the modeled REE enrichment and fractionation (see Text S4). The results of the models vary significantly but none of them reproduce both the incompatible element contents analyzed in the coarse-grained sample, and the corresponding fractionations between LREE and MREE or HREE (Figure S4). Therefore, crystallization only cannot explain the highest compositions in incompatible elements observed in the central coarse-grained layer, and the same conclusion also applies for the stronger enrichments observed elsewhere in the coarse-grained lithology.

Some amount of trapped melt crystallization might have happened during the late crystallization stage of the coarse-grained lithology, at the time of complete closure of the mush porosity. In order to test this hypothesis, we applied the equilibrium distribution method (EDM) of Bédard (1994) to calculate the fraction of trapped melt required to explain the deviation from the whole rock composition of each Cpx REE compositions analyzed in the central coarse-grained sample, where interactions with the intrusive magmas are supposed to remain minor (methodology detailed in Text S4). The results show that individually, each element content of all Cpx REE can be explained by up to ~5% of melt loss and up to ~11% of trapped melt excess in the mush (Figure 12a). These differences of gained/lost melt fractions required to reproduce the REE contents of various Cpx grains from a same thin section could highlight a heterogeneous cm-sized reorganization of interstitial melts within the coarse-grained mush prior to complete crystallization. However, the results also show that for a single Cpx grain, different melt fractions are required to explain each REE contents. Hence, although intra-sample trapped melt reorganization can account for some of the chemical heterogeneity, it fails to explain the Cpx REE fractionations, especially for minerals presenting the more enriched REE compositions (highest melt fractions), likely suggesting that an alternative process is ongoing.

At Atlantis Bank, anomalous mineral incompatible trace element enrichments and fractionations were described in various studies (Boulanger et al., 2020; Ferrando, France, et al., 2021; Gao et al., 2007; Lissenberg & MacLeod, 2016; Sanfilippo et al., 2020; Zhang et al., 2021) and attributed, together with the characteristic

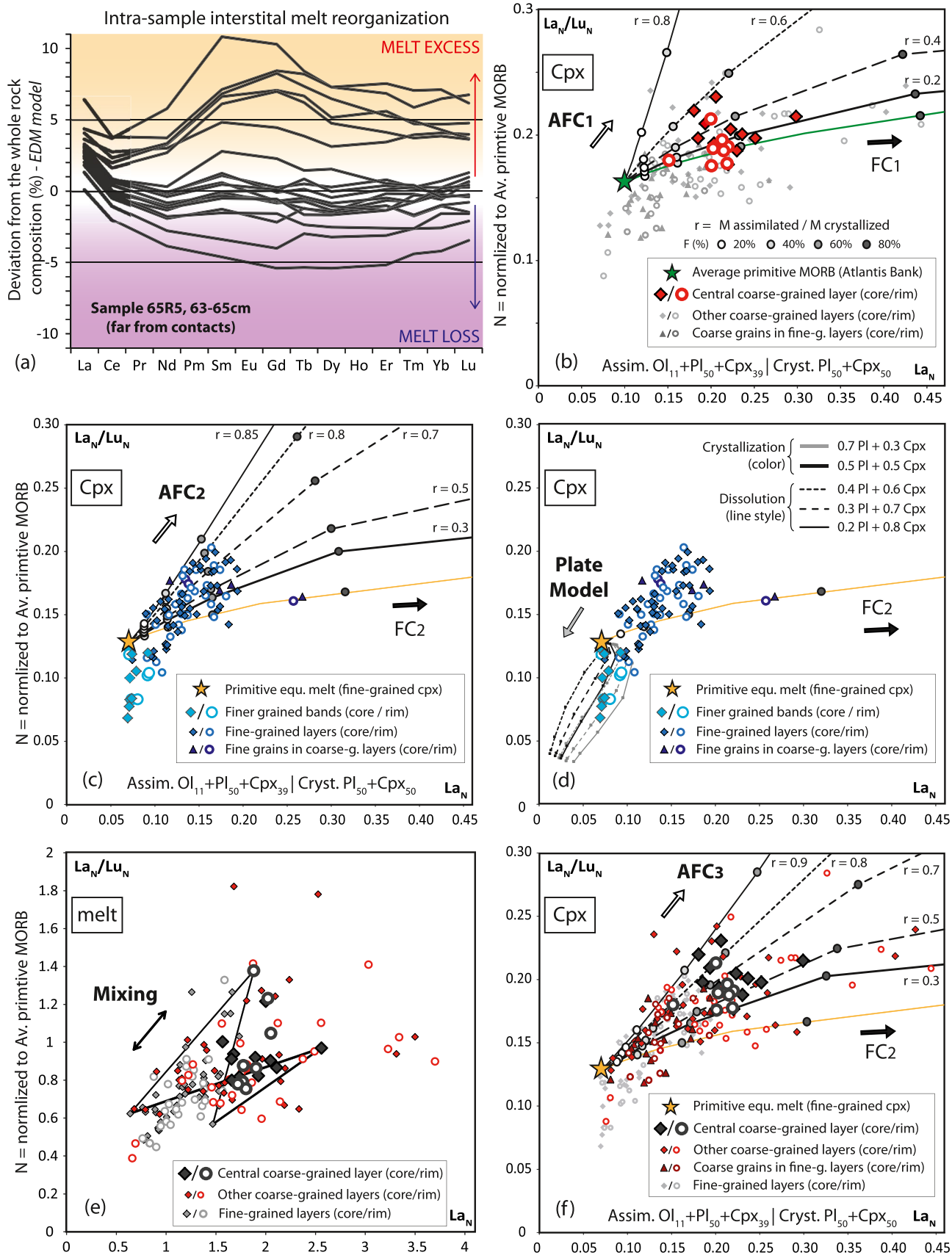
Intra-sample interstital melt reorganization
MELT EXCESS
MELT LOSS
Sample 65R5, 63-65cm
(far from contacts)
Deviation from the whole rock composition (%) - EDM model
(a)
La Ce Pr Nd Pm Sm Eu Gd Tb Dy Ho Er Tm Yb Lu
(b)
Cpx
AFC1
FC1
r = 0.8
r = 0.6
r = 0.4
r = 0.2
r = M assimilated / M crystallized
F (%) 20% 40% 60% 80%
Average primitive MORB (Atlantis Bank)
Central coarse-grained layer (core/rim)
Other coarse-grained layers (core/rim)
Coarse grains in fine-g. layers (core/rim)
N = normlized to Av. primtive MORB
Assim. Ol11+Pl50+Cpx39 | Cryst. Pl50+Cpx50
(c)
AFC2
FC2
r = 0.85
r = 0.7
r = 0.5
r = 0.3
Primitive equ. melt (fine-grained cpx)
Finer grained bands (core / rim)
Fine-grained layers (core/rim)
Fine grains in coarse-g. layers (core/rim)
(d)
Plate Model
Crystallization (color)
0.7 Pl + 0.3 Cpx
0.5 Pl + 0.5 Cpx
Dissolution (line style)
0.4 Pl + 0.6 Cpx
0.3 Pl + 0.7 Cpx
0.2 Pl + 0.8 Cpx
(e)
melt
Mixing
(f)
AFC3
r = 0.9
r = 0.8
r = 0.7
r = 0.5
r = 0.3

**Figure 12.**

samples textures, to RPF and interactions between mushy cumulates and a percolating reactive melt. Similar observations and conclusions were also derived from other lower crust sections at slow-spreading oceanic centers (e.g., Coogan et al., 2000; Leuthold et al., 2018), fast spreading centers (Leuthold et al., 2018; Lissenberg et al., 2013), or in other geodynamic contexts (e.g., Hepworth et al., 2020; Gleeson et al., 2021). The same mineral textures interpreted as resulting from RPF in these previous studies are observed in the coarse-grained layers studied herein, such as resorbed grain boundaries for Pl and Ol interpreted as evidence for partial dissolution (Figures 3a, 3b, 3d and 3e), or poikilitic Cpx containing the latter minerals and described as evidence for crystallization from the reactive melt (Figures 3d and 3e; see also Section 4.1). We tested the potential implications of RPF during the evolution of the coarse-grained lithology prior to intrusion by applying the assimilation-fractional crystallization model (AFC, DePaolo, 1981) to the system. This approach has been extensively applied in literature, and has shown to be reliable for such natural systems (e.g., Boulanger et al., 2020; Coogan et al., 2000; Ferrando, France, et al., 2021; Gao et al., 2007; Lissenberg et al., 2013; Sanfilippo et al., 2020; Zhang et al., 2021). Details on the model selection, on the reaction equations, and on the other input parameters are given in Text S4 and Table S6. In summary, interactions between an average primitive olivine gabbro mush for the coarse-grained material and a primitive melt by AFC (AFC1, Figure 12b) result in increasing the Cpx $La_N/Lu_N$ ratio with the increasing assimilation + crystallization and overall differentiation of the reactive melt. The AFC1 model manages to reproduce the entire range of fractionation represented by the Cpx $La_N/Lu_N$ ratios of the central coarse-grained layer applying different assimilation/crystallization ratios ($r$) in the equation, which reveal a predominant crystallization regime, with stronger assimilation components ($r = 0.6$) in some areas compared to others ($r = 0.2$) at the thin section scale. Such local heterogeneities were already reported for the Atlantis Bank, and for other oceanic plutonic sections (see above). These variations likely indicate either heterogeneous percolation at the sample scale, with stronger assimilation in areas of preferential reactive melt circulation, or changes in porosity as the reaction proceeded (see also Boulanger et al., 2020; Ferrando, France, et al., 2021). Porosity variations during the reaction may eventually result in progressive closing of the mush porosity preventing further infiltration of external melt, and favor larger amounts of crystallization.

Altogether, the best model explaining both the textures and geochemical characteristics of the coarse-grained lithology prior to intrusion is an evolution by heterogeneous RPF within an olivine gabbro-forming crystal mush (Figures 12b and 13, Step 1), even though late stage intra-sample (cm-scale) interstitial melt migration also likely occurred (Figure 12a).

#### 5.3.2. Evolution of the Fine-Grained Layers Post Intrusion

Compared to coarse-grained layers, no strong variability and related enrichment in REE is observed in the fine-grained lithology, with a maximum variation of a factor of 1.8 for Ce in Cpx in a single thin section. Nonetheless, fine-grained Cpx present comparable fractionations between light and heavy REE with slightly lower $La_N/Lu_N$ values ($La_N/Lu_N = 0.07–0.20$) than Cpx in the coarse-grained lithology ($La_N/Lu_N = 0.09–$

**Figure 12.** (a) Profiles representing for each rare earth element the trapped melt fraction required to mass balance the melt compositions in equilibrium with each Cpx analyzed in the central coarse-grained layer (~63 cm depth) back to its whole rock composition, thanks to the equations for the equilibrium distribution method (Bédard, 1994; Bédard et al., 2009). (b) $La_N/Lu_N$ ratio versus $La_N$ of Cpx from the central coarse-grained layer (far from contacts, red points). Values of other coarse-grained Cpx from the section represented in gray for comparison. Green curve: fractional crystallization (FC1) from the average primitive MORB composition (Cpx in equilibrium). Black curves: assimilation-fractional crystallization (AFC1) modeling RPF in the central coarse-grained layer for different ratios of mass assimilated/mass crystallized (r). F: relative mass of melt remaining during the reaction (as a fraction of the original melt mass). (c) and (d) $La_N/Lu_N$ ratio versus $La_N$ of Cpx from the fine-grained layers (dark blue points) and from the finer grained bands (light blue points, see Figure 10). Yellow curve: fractional crystallization (FC2) from the average least evolved equilibrium melts composition with Cpx analyzed in the fine-grained layers (yellow star, without considering the finer grained bands compositional range). (c) Black curves: assimilation-fractional crystallization (AFC2) modeling RPF in the fine-grained layers. See legend details in panel (b). (d) Gray and black curves: Plate model of reactive melt percolation associated with a chromatographic effect during transport for different modal compositions of dissolved and assimilated phases (Pl and Cpx, see legend and Text S5 for details). (e) $La_N/Lu_N$ ratio versus $La_N$ of melts in equilibrium with Cpx from the central coarse-grained layer (dark gray points), from the rest of the coarse-grained layers (red points), and from the fine-grained layers (away from the finer grained bands, lighter gray). Black curves are mixing curves between two end-member compositions from the fine-grained range and two of the most enriched and fractionated compositions analyzed in the central coarse-grained layer (see Text S6 and Table S6). (f) $La_N/Lu_N$ ratio versus $La_N$ of Cpx from the central coarse-grained layer (dark gray), from the other coarse-grained layers (red points) and from the enclaves of coarse-grained material in the fine-grained layers (darker red points). Cpx compositions from the fine-grained layers represented in light gray for comparison. Black curves: assimilation-fractional crystallization (AFC3) modeling RPF in the coarse-grained layers. See legend details in panel (b). All values in panels (b)–(f) are normalized to an average primitive MORB composition of the Atlantis Bank area (Table S5).

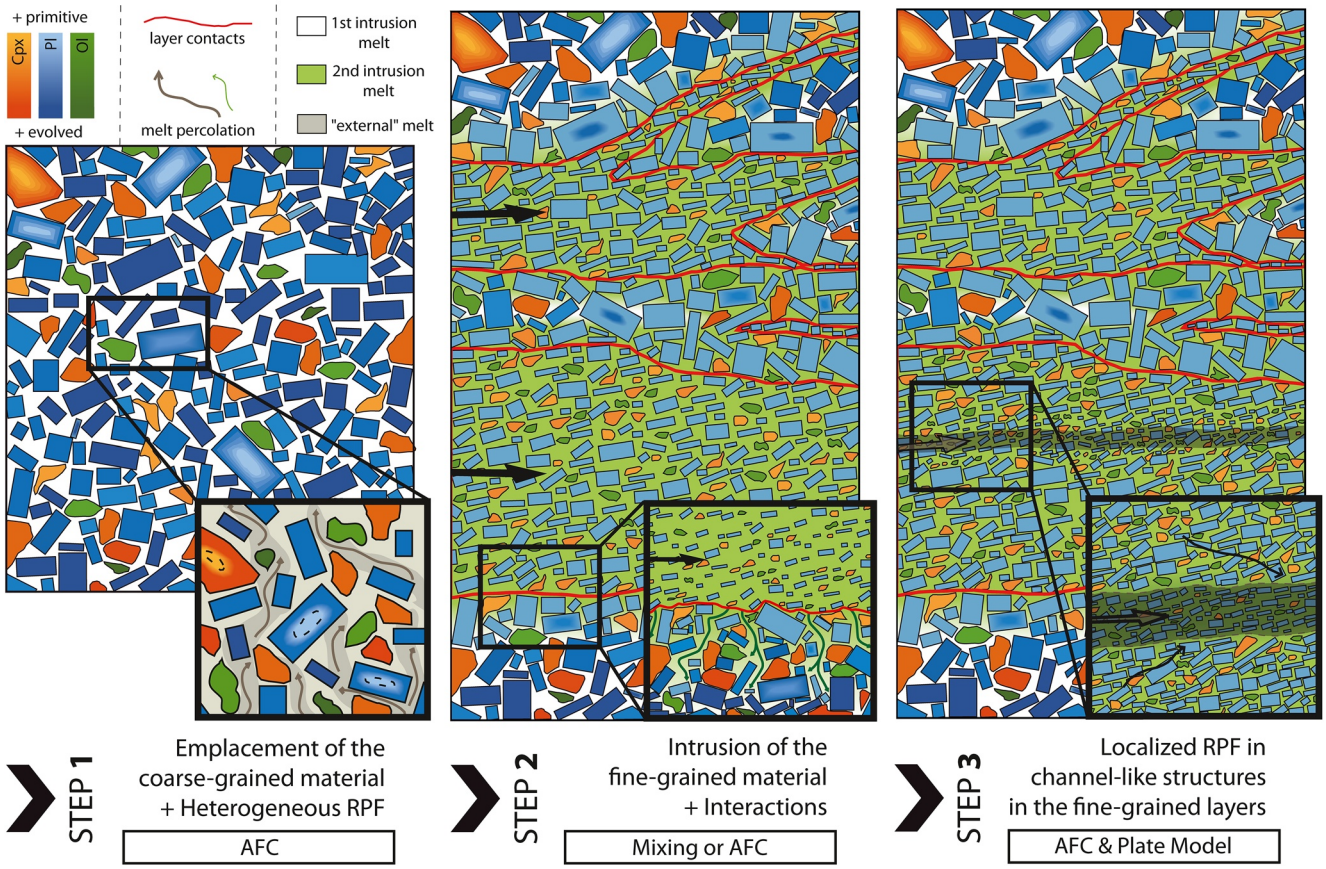


**Figure 13.** Schematic model of formation of the layered section U1473A-65R5. Step 1: crystallization of the coarse-grained mush and widespread but heterogeneous reactive percolation of a primitive melt (darker areas and gray arrows in the outset enlarged view) resulting in incompatible trace element fractionation and enrichment of the minerals. Step 2: intrusion of a crystal-bearing magma within the coarse-grained mush that is already at an advanced stage of solidification. Liquid from the intruding magma (green) infiltrates the coarse-grained material, which leads to mixing with any residual melt trapped in porosity (white) and/or interactions with the coarse-grained crystal matrix. Step 3: localization of the porous flow within channel-like structures in the fine-grained material (darker area) forms finer grained bands that progressively transition to the fine-grained material. Incompatible element contents become strongly fractionated in those domains due to a chromatographic effect during melt migration.

0.28, Figure 12c). We modeled the evolution by fractional crystallization of a parental melt equivalent to fine-grained layers (without considering the finer grained bands, see Text S5 and Table S6). As for the coarse-grained material, the results also show that the highest REE contents are reproduced after more than 70% crystallization and the modeled $La_N/Lu_N$ are still lower than the majority of the analyzed Cpx values (Figure 12c). In addition, the Cpx Ti contents are higher than expected at equivalent Mg# (Figure 11), and the fine-grained olivine gabbros present characteristic textures that we interpret as resulting from RPF (Figures 3g–3l). Those specific textural features are mainly Pl and Cpx presenting resorbed grain boundaries, indicating assimilation, or overgrowths at the expanse of surrounding minerals (Figures 3h, 3k and 3l), indicating crystallization during the reactions. To test the potential effect of a RPF process on the fine-grained layer compositions, we applied a second AFC reaction (AFC2 model) to test the effect of a reaction between an average primitive olivine gabbro mush (for the fine-grained material) and a primitive melt, taken as the average melt in equilibrium with Cpx from the fine-grained lithology presenting the most depleted values in REE (see Text S5 for details on the justification and input parameters of the model). The results show that the REE fractionation range of fine-grained layers can be explained by such melt-mush reactions considering assimilation/crystallization ratios ($r$) of up to 0.8 (Figure 12c). However, this model and a similar AFC process cannot explain the specific Cpx REE signatures of the finer grained bands present within fine-grained layers (e.g., Figure 10).

#### 5.3.3. Formation of the Finer Grained Bands in the Fine-Grained Layers

The finer grained bands identified in fine-grained layers present distinct geochemical signatures characterized by depletion in the most incompatible light REEs, which is opposite to what is expected after an evolution by AFC as described in the rest of the fine-grained layers (see the above Section 5.3.2). Formation of the finer grained bands by secondary intrusions of material within the fine-grained layers can be discarded because (a) despite the localized fractionated trace element signatures, major element contents of the finer grained areas are the same as in the rest of the fine-grained layers (e.g., Figure 9), (b) the transition between fine-grained material and the finer grained bands is gradual (no clear intrusive contact is detected), and (c) the thickness of the finer grained bands is very limited (<2 cm width).

The stronger depletion in the more incompatible REE can be explained by a chromatographic effect (Godard et al., 1995; Navon & Stopler, 1985; Vernières et al., 1997) during migration of an interstitial melt within a crystal matrix. Given that light REE move faster than heavy REE with the melt, the reaction would result in preferential depletion in the most incompatible elements in the products that reacted the most. In order to test the involvement of a chromatographic effect, we applied the Plate Model to the system (Vernières et al., 1997; details in Text S5). The reaction involves dissolution of mostly Cpx and minor Pl (between 60% and 80% Cpx and associated 40%–20% Pl), and crystallization of both Pl and Cpx (between 50% and 70% Pl, 50% and 30% Cpx). It results in a significant decrease of the La/Lu ratio and a decrease in the La content of the melt (Figure 12d). The decrease of Pl dissolved proportions (i.e., increasing dissolution Cpx/Pl ratios) is associated with lower La contents in the reactive melt and thus can account for lower La/Lu ratios in the reaction products. The REE signatures of the three finer-grained bands, with depletion in the most incompatible REE are therefore likely the consequence of evolution by RPF associated with a chromatographic component. Variations of the dissolved assemblages likely account for the slight local heterogeneities of the modal compositions throughout the bands, or may be linked to the compositional evolution of the melt during the reaction and thus its ability to dissolve the minerals encountered.

Overall, the presence of the finer grained bands can be explained by the formation of preferential channels of melt percolation through the lithology (Figure 13, Step 3). In order to create such localized flow, the rest of the fine-grained material was likely at an advanced stage of crystallization, with this final step of RPF occurring during the last step of formation of the section. This model is consistent with the stronger magmatic deformation observed in the finer grained bands (higher *J*, *F*, *L* indexes; Figure 5f), and associated potential reinforcement of the pre-existing fabric by magmatic deformation in areas of localized melt flow.

#### 5.3.4. Interactions at the Layer Contacts—Direct Consequences of the Intrusion

Infiltration of the intrusive fine-grained material within the intruded coarse-grained one is highlighted by the presence of interstitial fine-grained material incursions within the coarse-grained mush close to the sharp intrusive contacts, and by the diffuse nature of intrusive contacts between some layers (Figures 2c and 4). In addition, the composition of the coarse-grained layers close to contacts, which trends toward the most depleted values of the fine-grained layers (see Section 4.5, Figure 9), also suggests that the infiltrating magma interacted to some extent with the coarse-grained solidifying mush. In order to better constrain the interaction process, two different theoretical models have been considered: (a) the infiltrating magma from the fine-grained layers mixed with the interstitial melt from the intruded mush before crystallizing; (b) the infiltrating magma reacted with the already formed minerals of the coarse-grained mush, dissolving them and crystallizing a new generation of minerals with homogenized compositions.

We first modeled a simple mixing process between (a) two end-member melts in equilibrium with the most enriched and fractionated Cpx from the central part of the larger coarse-grained layer, and (b) two primitive melts in equilibrium with the fine-grained Cpx (excluding the finer grained bands; Figure 12e and Text S6). The results show that most of the equilibrium melts REE contents can be explained by mixing. However, the most enriched and fractionated values are not reproduced by the mixing process alone. Together with numerous textural features indicative of RPF, especially close to contacts (Figures 4d and 4e), the intrusion likely led to RPF processes within the coarse-grained mush. We modeled the corresponding RPF process with an AFC model (AFC3 model) that considers the interaction between a primitive olivine gabbro mush for the coarse-grained material, with an primitive parental melt equivalent to the fine-grained lithology

(details in Text S6). The results show that such a reaction can produce the full chemical range of the coarse-grained material likely affected by the infiltration (Figure 12f).

Altogether, the formation of the coarse-grained lithology is likely the consequence of two steps of interactions with percolating melts, one prior to, and the second linked directly to the intrusive event (Figure 13, step 1 and 2), although the mixing hypothesis with further differentiation cannot be completely discarded. The first step of RPF linked to the evolution of the coarse-grained mush impacted the REE composition of the minerals, which was then likely partially erased after the intrusion event. Finally, the lack of systematic mineral zoning in trace element contents either reflects heterogeneous percolation and the uneven distribution of RPF signatures in the samples, or is the direct consequence of the homogenization process, which partially erased the initial signatures.

## 6. Implications for Melt Migration Processes During the Evolution of Lower Crustal Magma Reservoirs

Grain size variations between fine-grained "micrograbbros" and coarse-grained olivine gabbros were reported in ODP Hole 735B (Dick, Kvassnes, et al., 2019; Dick, Meyer, et al., 1991), and studied in detail by Bloomer et al. (1991). Two types of recurrent grain size variations are reported in crustal sections drilled at Atlantis Bank (MacLeod et al., 2017b): Discrete layers with planar, mostly sharp intrusive relationships such as the one studied herein, and irregular patchy pods of mixed microgabbros and olivine gabbros that are present on average every 4 m in IODP Hole U1473A (Ferrando, France, et al., 2021). Bloomer et al. (1991) studied both types of grain size variations and inferred two main processes for the formation of the layering and the patchy structures: (a) changes of crystallization conditions and subsequent nucleation and growth rates, and (b) the occurrence of intrusions of crystal mushes or redistribution of crystal density by development of crystal-rich plumes or local slumps of material, both occurring at the border of an irregularly shaped magma chamber. Interestingly, they also qualified the finer grained lithology as "intrusive in a local sense" as in the model developed herein and in Ferrando, France, et al. (2021), and hypothesized that the distinct lithologies potentially had initially different cumulus compositions now "erased by intermingling of intercumulus liquids and re-equilibration," a process very similar to the homogenization process documented herein. Ferrando, France, et al. (2021) and Ferrando, Basch, et al. (2021) focused on the patchy gabbros, which they describe as formed by segregation of residual melt from RPF occurring within a crystal mush (coarse-grained domains) into more evolved melt pockets that ultimately form the fine-grained patchy cumulate domains in the host coarse-grained gabbro. Altogether, both the latter study and ours reveal the complex history of mush evolution in oceanic magma reservoirs, but also tend to show the strong if not ubiquitous involvement of RPF and melt-mush reactions during the course of melt differentiation, and migration.

The whole-round core images allow us to compare the dip directions of the successive layers (Figures 2b, 14a and 14b). A planar contact is represented by a sinusoidal trace on the whole-round image, with the dip direction given by the azimuth of the sinusoid minimum (Figure 14a). The whole round image of section 65R5 shows that the successive layers are heterogeneously organized in three dimensions, with the two fine-grained layers at the top of the section displaying subparallel margins (~2–10 cm and ~25–43 cm depth in the section), the third pinching out toward the front of the core (~82–98 cm depth), and the fourth pinching out toward the back of the core (~110–117 cm depth, Figure 14b). The whole-round image also suggests that the two fine-grained layers at the top of the section likely merge together backward of the core, and the central coarse-grained layer also pinches out backward. These structural features indicate that the lateral extent of the layers described herein is not at the scale of several meters, but likely represent an interfingered contact between two larger intrusions (Figures 14b–14d). Such an intrusion of a more primitive magma into a mush recalls geophysical observations of magma sills stacked at various depths and different stages of crystallization, with thicknesses ranging from tens to hundreds of meters (Canales et al., 2017). The exact lateral extent of the structure and the size of the intrusive bodies are difficult to establish. Yet, our interpretation tentatively explains why such regular layering is not ubiquitous at IODP Hole U1473A (Figure 2a) as the number of magma bodies emplaced in the accreting crust was likely limited (e.g., Dick et al., 2019; Dick et al., 2000), besides the fact that such structures are poorly preserved due to subsequent overprinting as a result of plastic deformation (MacLeod et al., 2017b). In this perspective, the two areas of

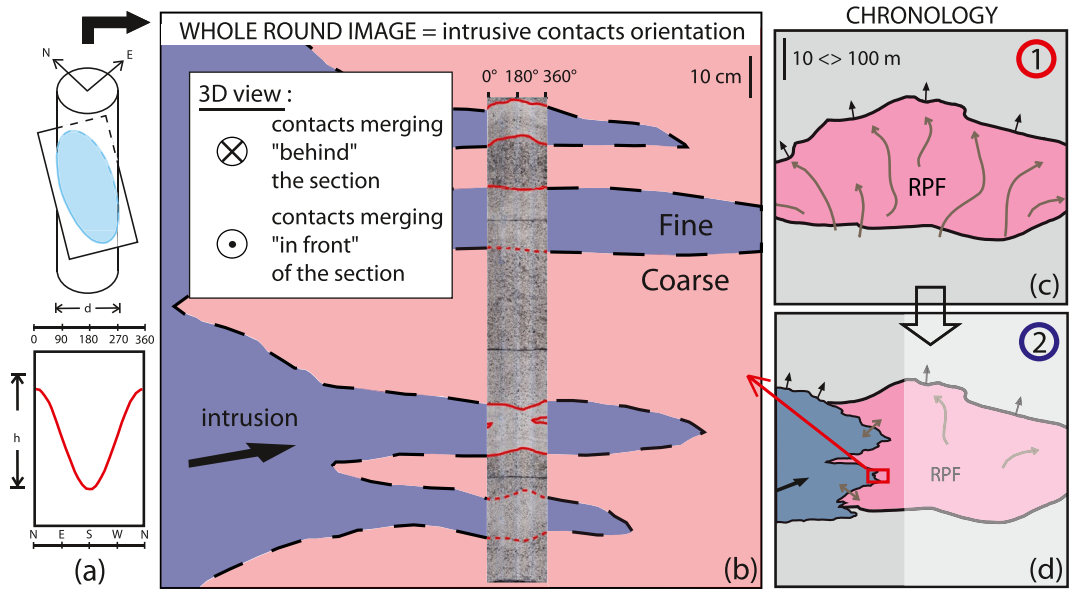


**Figure 14.** Integrated model of formation of the layered series in section U1473A-65R5. (a) Interpretation scheme of the geometric features present in the whole-round scan of a drilled core (here, schematically, a plane crosscutting the core at a 45° angle). (b) Interpretation of the layered geometry of the section and the contacts between the two crosscutting lithologies. (c) First step of formation: crystallization of the initial mush (formation of the coarse-grained lithology, red) and differentiation constrained by RPF (gray arrows). Black arrows: melts escaping from the open-system mush due to buoyancy, compaction, and/or deformation. (d) Second step of formation: intrusion of the crystal-bearing magma, leading to the formation of the fine-grained lithology (purple). Double gray arrows: interactions and homogenization at the contact of the two lithologies.

IODP Hole U1473A where layers are particularly present (around 150, and around 600 mbsf, Figure 2) may represent two areas of contacts between larger plutonic units.

## 7. Conclusions

This study, conducted on Atlantis Bank samples, is the first high-resolution petrographic, microstructural, and geochemical study of olivine gabbro layers from slow-spreading lower oceanic crust. We show that both types of melt migration by RPF and intrusion were likely involved in the formation of the studied section. The layering is defined by grain size variations, and results from the intrusion of a crystal-bearing magma within an almost solidified mush. The limited lateral extent of the structure, determined thanks to the geometry of the contacts, petrostructures, together with the chemical differences between the fine- and the coarse-grained layers suggest that the layering likely represents an interfingered contact between two larger intrusions. Our study also emphasizes the importance of melt migration and associated interaction processes during magma emplacement at the ridge axis, and suggests that reactive melt percolation is ubiquitous during the formation of the layered section studied here.

Petrographic observations and geochemical analyses combined to numerical modeling enabled us to characterize the processes most likely involved in the evolution of both lithologies. During the first step of evolution of the coarse-grained mush prior to intrusion, widespread melt migration occurred heterogeneously (at the sample scale) by RPF, leading to incompatible element fractionation and enrichments of the minerals. The intrusion itself led to the emplacement of the more primitive, fine-grained layers parental magma in the section that also percolated through and interacted with the coarse-grained mush at contacts. This step led to the partial overprint of the initial magmatic signatures of the coarse-grained lithology and local homogenization of chemical signatures either by melt mixing or partial assimilation-crystallization. Post-intrusion, the fine-grained gabbro cumulates mostly evolved following a RPF process likely similar to that recorded in the preserved coarse-grained layer. The last step of evolution of the fine-grained olivine

gabbro layers involved migration of interstitial melts in cm-scale structures, and led to the development of light REE depleted signatures enhanced by a chromatographic effect during melt migration.

The different types of numerical models required to better constrain the reactions also potentially illustrate that the consequences of RPF depend on the distribution and modalities of melt migration. Whereas widespread reactive melt percolation can be simulated thanks to an AFC model (DePaolo, 1981), localized and focused reactive melt percolation was better reproduced by the Plate Model (Vernières et al., 1997). The superposition of geochemical signatures from successive magmatic processes on the studied 1.3 m-long section was only resolved thanks to the high-resolution approach, and because the section was preserved from subsequent alteration or crystal-plastic deformation. Finally, although the grain-size variations described here are not ubiquitous along the drilled core, similar structural, textural and geochemical observations have been reported in other drilled sections from Atlantis Bank, and in other slow-spreading oceanic plutonic sections. The intrusion and reactive melt percolation processes described herein therefore likely represent key processes to take into account for the formation of the lower crust.

## Data Availability Statement

All major and trace element data used in this study are available at the OTELo Research Data Repository—ORDaR (Table S3—https://doi.org/10.24396/ORDAR-85 and Table S4—https://doi.org/10.24396/ORDAR-86) or in Supporting Information S1.

**Acknowledgments**
The authors express our warm thanks to the various people involved at different technical stages in this work: C. Nevado and D. Delmas (Geosciences Montpellier) for their high quality thin sections, and Jean-Luc Devidal (LMV) and Fabrice Barou (Geosciences Montpellier) for their assistance during EPMA and EBSD measurements, respectively. This research used data provided by the International Ocean Discovery Program (IODP). The authors gratefully acknowledge the Captain and shipboard crew of IODP Expedition 360 for their assistance in data collection at sea. The authors wish to thank the Scientific Party of IODP Expedition 360 for fruitful discussions during the cruise and post-cruise meeting. This study also benefited from discussions with David Jousselin (CRPG), and Kathi Faak (RUB), and from thorough comments by M. Edmonds, L. A. Coogan, G. Borghini, B. Hayes, J. H. Bédard, and two anonymous reviewers. The authors thank Robert Dennen for English phrasing improvements. This is CRPG contribution number 2797. This research was supported by CNRS-INSU and IODP-France. M. Boulanger's PhD project was funded by the French Ministry of Research (MESRI). Open access funding enabled and organized by Projekt DEAL.

## References

Baines, A. G., Cheadle, M. J., Dick, H. J. B., Scheirer, A. H., John, B. E., Kusznir, N. J., & Matsumoto, T. (2003). Mechanism for generating the anomalous uplift of oceanic core complexes: Atlantis Bank, southwest Indian Ridge. *Geology*, *31*(12), 1105–1108. https://doi.org/10.1130/G19829.1

Baines, A. G., Cheadle, M. J., John, B. E., & Schwartz, J. J. (2008). The rate of oceanic detachment faulting at Atlantis Bank, SW Indian Ridge. *Earth and Planetary Science Letters*, *273*(1–2), 105–114. https://doi.org/10.1016/j.epsl.2008.06.013

Basch, V., Rampone, E., Crispini, L., Ferrando, C., Ildefonse, B., & Godard, M. (2019). Multi-stage reactive formation of troctolites in slow-spreading oceanic lithosphere (Erro-Tobbio, Italy): A Combined field and petrochemical study. *Journal of Petrology*, *60*(5), 873–906. https://doi.org/10.1093/petrology/egz019

Bédard, J. H. (1994). A procedure for calculating the equilibrium distribution of trace elements among the minerals of cumulate rocks, and the concentration of trace elements in the coexisting liquids. *Chemical Geology*, *118*, 143–153. https://doi.org/10.1016/0009-2541(94)90173-2

Bédard, J. H. (2015). Ophiolitic magma chamber processes, a perspective from the Canadian Appalachians. In B. Charlier, O. Namur, R. Latypov, & C. Tegner (Eds.), *Layered intrusions* (pp. 1–748). Springer. https://doi.org/10.1007/978-94-017-9652-1

Bédard, J. H., Hébert, R., Berclaz, A., & Varfalvy, V. (2000). Syntexis and the genesis of lower oceanic crust. *Special Papers—Geological Society of America*, *349*, 105–119. https://doi.org/10.1130/0-8137-2349-3.105

Bédard, J. H., Leclerc, F., Harris, L. B., & Goulet, N. (2009). Intra-sill magmatic evolution in the Cummings Complex, Abitibi greenstone belt: Tholeiitic to calc-alkaline magmatism recorded in an Archaean subvolcanic conduit system. *Lithos*, *111*(1–2), 47–71. https://doi.org/10.1016/j.lithos.2009.03.013

Blackman, D. K., Ildefonse, B., John, B., Ohara, Y., Miller, D. J., & Macleod, C. J. (2006). Site U1309. *Proceedings of the IODP*. https://doi.org/10.2204/iodp.proc.304305.103.2006

Bloomer, S. H., Meyer, P. S., Dick, H. J. B., Ozawa, K., & Natland, J. H. (1991). Textural and mineralogic variations in gabbroic rocks from Hole 735B. *Proceedings of the Ocean Drilling Program*.

Borghini, G., Francomme, J. E., & Fumagalli, P. (2018). Melt-dunite interactions at 0.5 and 0.7 GPa: Experimental constraints on the origin of olivine-rich troctolites. *Lithos*, *323*, 44–57. https://doi.org/10.1016/j.lithos.2018.09.022

Borghini, G., & Rampone, E. (2007). Postcumulus processes in oceanic-type olivine-rich cumulates: The role of trapped melt crystallization versus melt/rock interaction. *Contributions to Mineralogy and Petrology*, *154*(6), 619–633. https://doi.org/10.1007/s00410-007-0217-5

Boulanger, M., France, L., Deans, J. R., Ferrando, C., Lissenberg, J. C., & von der Handt, A. (2020). Magma reservoir formation and evolution at a slow-spreading center (Atlantis Bank, Southwest Indian Ridge). *Frontiers in Earth Science*, *8*. https://doi.org/10.3389/feart.2020.554598

Canales, J. P., Dunn, R. A., Arai, R., & Sohn, R. A. (2017). Seismic imaging of magma sills beneath an ultramafic-hosted hydrothermal system. *Geology*, *45*(5), 451–454. https://doi.org/10.1130/G38795.1

Cann, J. R., Blackman, D. K., Smith, D. K., McAllister, E., Janssen, B., Mello, S., et al. (1997). Corrugated slip surfaces formed at ridge-transform intersections on the mid-Atlantic ridge. *Nature*, *385*(6614), 329–332. https://doi.org/10.1038/385329a0

Casey, J. F., Banerji, D., & Zarian, P. (2007). Leg 179 synthesis: Geochemistry, stratigraphy, and structure of gabbroic rocks drilled in ODP Hole 1105A, Southwest Indian Ridge. In *Proceedings of the Ocean Drilling Program, Scientific Results*. Ocean Drilling Program College Station. https://doi.org/10.2973/odp.proc.sr.179.001.2007

Cheadle, M. J., & Gee, J. S. (2017). Quantitative textural insights into the formation of gabbro in mafic Intrusions. *Elements*, *13*(6), 409–414. https://doi.org/10.2138/gselements.13.6.409

Collier, M. L., & Kelemen, P. B. (2010). The case for reactive crystallization at mid-ocean ridges. *Journal of Petrology*, *51*(9), 1913–1940. https://doi.org/10.1093/petrology/egq043

Coogan, L. A., MacLeod, C. J., Dick, H. J. B., Edwards, S. J., Kvassnes, A., Natland, J. H., et al. (2001). Whole-rock geochemistry of gabbros from the Southwest Indian Ridge: Constraints on geochemical fractionations between the upper and lower oceanic crust and magma chamber processes at (very) slow-spreading ridges. *Chemical Geology*, *178*(1–4), 1–22. https://doi.org/10.1016/S0009-2541(00)00424-1

Coogan, L. A., Saunders, A. D., Kempton, P. D., & Norry, M. J. (2000). Evidence from oceanic gabbros for porous melt migration within a crystal mush beneath the Mid-Atlantic Ridge. *Geochemistry, Geophysics, Geosystems*, *1*(9). https://doi.org/10.1029/2000GC000072

Coogan, L. A., Thompson, G. M., MacLeod, C. J., Dick, H. J. B., Edwards, S. J., Hosford Scheirer, A., & Barry, T. L. (2004). A combined basalt and peridotite perspective on 14 million years of melt generation at the Atlantis Bank segment of the Southwest Indian Ridge: Evidence for temporal changes in mantle dynamics? *Chemical Geology*, *207*(1–2), 13–30. https://doi.org/10.1016/j.chemgeo.2004.01.016

DePaolo, D. J. (1981). Trace element and isotopic effects of combined wallrock assimilation and fractional crystallization. *Earth and Planetary Science Letters*, *53*(2), 189–202. https://doi.org/10.1016/0012-821X(81)90153-9

Dick, H. J. B., Kvassnes, A. J. S., Robinson, P. T., MacLeod, C. J., & Kinoshita, H. (2019). The Atlantis Bank Gabbro Massif, Southwest Indian Ridge. *Progress in Earth and Planetary Science*, *6*(1), 64. https://doi.org/10.1186/s40645-019-0307-9

Dick, H. J. B., Lin, J., & Schouten, H. (2003). An ultraslow-spreading class of ocean ridge. *Nature*, *426*(6965), 405–412. https://doi.org/10.1038/nature02128

Dick, H. J. B., MacLeod, C. J., Blum, P., Abe, N., Blackman, D. K., Bowles, J. A., et al. (2019). Dynamic accretion beneath a slow-spreading ridge segment: IODP Hole 1473A and the Atlantis Bank oceanic core complex. *Journal of Geophysical Research: Solid Earth*, *124*(12), 12631–12659. https://doi.org/10.1029/2018JB016858

Dick, H. J. B., Meyer, P. S., Bloomer, S., Kirby, S., Stakes, D. & Mawer, C. (1991). Lithostratigraphic evolution of an in-situ section of oceanic layer 3. Proceedings of the Ocean Drilling Program Scientific Results, 118. https://doi.org/10.2973/odp.proc.sr.118.128.1991

Dick, H. J. B., Natland, J. H., Alt, J. C., Bach, W., Bideau, D., Gee, J. S., et al. (2000). A long in situ section of the lower ocean crust: Results of ODP Leg 176 drilling at the Southwest Indian Ridge. *Earth and Planetary Science Letters*, *179*(1), 31–51. https://doi.org/10.1016/S0012-821X(00)00102-3

Dick, H. J. B., Natland, J. H., & Miller, D. J. (1999). Shipboard Scientific Party (1999): Site 735B. *Proceedings of the Ocean Drilling Program*.

Dick, H. J. B., Ozawa, K., Meyer, P. S., Niu, Y., Robinson, P. T., Constantin, M., et al. (2002). 10. Primary silicate mineral chemistry of a 1.5-km section of very slow spreading lower ocean crust: ODP Hole 753B, Southwest Indian Ridge. *Proceedings of the Ocean Drilling Program: Scientific Results*, *176*, 1–61.

Dick, H. J. B., Schouten, H., Meyer, P. S., Gallo, D. G., Bergh, H., Tyce, R., et al. (1991). Tectonic evolution of the Atlantis II fracture zone. *Proceedings of the Ocean Drilling Program, Scientific Results*, *118*, 359–398. https://doi.org/10.2973/odp.proc.sr.118.156.1991

Drouin, M., Godard, M., Ildefonse, B., Bruguier, O., & Garrido, C. J. (2009). Geochemical and petrographic evidence for magmatic impregnation in the oceanic lithosphere at Atlantis Massif, Mid-Atlantic Ridge (IODP Hole U1309D, 30°N). *Chemical Geology*, *264*(1–4), 71–88. https://doi.org/10.1016/j.chemgeo.2009.02.013

Dunn, R. A., Lekić, V., Detrick, R. S., & Toomey, D. R. (2005). Three-dimensional seismic structure of the Mid-Atlantic Ridge (35°N): Evidence for focused melt supply and lower crustal dike injection. *Journal of Geophysical Research: Solid Earth*, *110*(9), 1–17. https://doi.org/10.1029/2004JB003473

Escartín, J., Smith, D. K., Cann, J., Schouten, H., Langmuir, C. H., & Escrig, S. (2008). Central role of detachment faults in accretion of slow-spreading oceanic lithosphere. *Nature*, *455*, 790–794. https://doi.org/10.1038/nature07333

Feig, S. T., Koepke, J., & Snow, J. E. (2010). Effect of oxygen fugacity and water on phase equilibria of a hydrous tholeiitic basalt. *Contributions to Mineralogy and Petrology*, *160*(4), 551–568. https://doi.org/10.1007/s00410-010-0493-3

Ferrando, C., Basch, V., Ildefonse, B., Deans, J. R., Sanfilippo, A., Barou, F., & France, L. (2021). Compaction-driven melt extraction and accumulation in a slow-spreading oceanic crust: Microstructures of olivine gabbros from Atlantis Bank (IODP hole U1473A, SWIR). *Tectonophysics*, *815*, 229001.

Ferrando, C., France, L., Basch, V., Sanfilippo, A., Tribuzio, R., & Boulanger, M. (2021). Grain size variations record segregation of residual melts in slow-spreading oceanic crust (Atlantis Bank, 57°E Southwest Indian Ridge). *Journal of Geophysical Research: Solid Earth*, *126*(4), e2020JB020997.

Ferrando, C., Godard, M., Ildefonse, B., & Rampone, E. (2018). Melt transport and mantle assimilation at Atlantis Massif (IODP Site U1309): Constraints from geochemical modeling. *Lithos*, *323*, 24–43. https://doi.org/10.1016/j.lithos.2018.01.012

Gale, A., Dalton, C. A., Langmuir, C. H., Su, Y., & Schilling, J. G. (2013). The mean composition of ocean ridge basalts. *Geochemistry, Geophysics, Geosystems*, *14*(3), 489–518. https://doi.org/10.1029/2012GC004334

Gao, Y., Hoefs, J., Hellebrand, E., von der Handt, A., & Snow, J. E. (2007). Trace element zoning in pyroxenes from ODP Hole 735B gabbros: Diffusive exchange or synkinematic crystal fractionation? *Contributions to Mineralogy and Petrology*, *153*(4), 429–442. https://doi.org/10.1007/s00410-006-0158-4

Gleeson, M. L. M., Gibson, S. A., & Stock, M. J. (2021). Upper mantle mush zones beneath low melt flux ocean island volcanoes: Insights from Isla Floreana, Galapagos. *Journal of Petrology*, *61*, 1–26. https://doi.org/10.1093/petrology/egaa094

Godard, M., Awaji, S., Hansen, H., Hellebrand, E., Brunelli, D., Johnson, K., et al. (2009). Geochemistry of a long in-situ section of intrusive slow-spread oceanic lithosphere: Results from IODP Site U1309 (Atlantis Massif, 30°N Mid-Atlantic-Ridge). *Earth and Planetary Science Letters*, *279*(1–2), 110–122. https://doi.org/10.1016/j.epsl.2008.12.034

Godard, M., Bodinier, J. L., & Vasseur, G. (1995). Effects of mineralogical reactions on trace element redistributions in mantle rocks during percolation processes: A chromatographic approach. *Earth and Planetary Science Letters*, *133*(3–4), 449–461. https://doi.org/10.1016/0012-821X(95)00104-K

Grimes, C. B., John, B. E., Cheadle, M. J., & Wooden, J. L. (2008). Protracted construction of gabbroic crust at a slow spreading ridge: Constraints from $^{206}Pb/^{238}U$ zircon ages from Atlantis Massif and IODP Hole U1309D (30°N, MAR). *Geochemistry, Geophysics, Geosystems*, *9*(8). https://doi.org/10.1029/2008GC002063

Hart, S. R., Blusztajn, J., Dick, H. J. B., Meyer, P. S., & Muehlenbachs, K. (1999). The fingerprint of seawater circulation in a 500-meter section of ocean crust gabbros. *Geochimica et Cosmochimica Acta*, *63*(23–24), 4059–4080. https://doi.org/10.1016/S0016-7037(99)00309-9

Hepworth, L. N., Kaufmann, F. E. D., Hecht, L., Gertisser, R., & O'Driscoll, B. (2020). Braided peridotite sills and metasomatism in the Rum Layered Suite, Scotland. *Contributions to Mineralogy and Petrology*, *175*(2), 1–25. https://doi.org/10.1007/s00410-019-1652-9

Hertogen, J., Emmermann, R., Robinson, P. T., & Erzinger, J. (2002). Lithology, mineralogy, and geochemistry of the lower ocean crust, ODP Hole 735B, Southwest Indian Ridge. *Proceedings of the Ocean Drilling Program Scientific Results, 176*. https://doi.org/10.2973/odp.proc.sr.176.003.2002

Higgie, K., & Tommasi, A. (2012). Feedbacks between deformation and melt distribution in the crust-mantle transition zone of the Oman ophiolite. *Earth and Planetary Science Letters*, *359*(360), 61–72. https://doi.org/10.1016/j.epsl.2012.10.003

Holm, P. M. (2002). Data report: On the composition of the lower ocean crust—Major and trace element analyses of gabbroic rocks from Hole 735B, 500–1500 mbsf. *Proceedings of the Ocean Drilling Program, 176 Scientific Results*. https://doi.org/10.2973/odp.proc.sr.176.020.2002

Holness, M. B., Hallworth, M. A., Woods, A., & Sides, R. E. (2007). Infiltration metasomatism of cumulates by intrusive magma replenishment: The wavy horizon, Isle of Rum, Scotland. *Journal of Petrology*, *48*(3), 563–587. https://doi.org/10.1093/petrology/egl072

Husen, A., Almeev, R. R., & Holtz, F. (2016). The effect of $H_2O$ and pressure on multiple saturation and liquid lines of descent in basalt from the Shatsky Rise. *Journal of Petrology*, *57*(2), 309–344. https://doi.org/10.1093/petrology/egw008

Ildefonse, B., Blackman, D. K., John, B. E., Ohara, Y., Miller, D. J., MacLeod, C. J., et al. (2007). Oceanic core complexes and crustal accretion at slow-spreading ridges. *Geology*, *35*(7), 623–626. https://doi.org/10.1130/G23531A.1

Irvine, T. N. (1982). Terminology for layered intrusions. *Journal of Petrology*, *23*, 127–162. https://doi.org/10.1093/petrology/23.2.127-a

Jian, H., Singh, S. C., Chen, Y. J., & Li, J. (2017). Evidence of an axial magma chamber beneath the ultraslow-spreading Southwest Indian Ridge. *Geology*, *45*(2), 143–146. https://doi.org/10.1130/G38356.1

Jousselin, D., Morales, L. F. G., Nicolle, M., & Stephant, A. (2012). Gabbro layering induced by simple shear in the Oman ophiolite Moho transition zone. *Earth and Planetary Science Letters*, *331–332*, 55–66. https://doi.org/10.1016/j.epsl.2012.02.022

Koepke, J., Botcharnikov, R. E., & Natland, J. H. (2018). Crystallization of late-stage MORB under varying water activities and redox conditions: Implications for the formation of highly evolved lavas and oxide gabbro in the ocean crust. *Lithos*, *323*, 58–77. https://doi.org/10.1016/j.lithos.2018.10.001

Koepke, J., Feig, S. T., & Snow, J. (2005). Hydrous partial melting within the lower oceanic crust. *Terra Nova*, *17*(3), 286–291. https://doi.org/10.1111/j.1365-3121.2005.00613.x

Lagabrielle, Y., Vitale Brovarone, A., & Ildefonse, B. (2015). Fossil oceanic core complexes recognized in the blueschist metaophiolites of Western Alps and Corsica. *Earth-Science Reviews*, *141*, 1–26. https://doi.org/10.1016/j.earscirev.2014.11.004

Leuthold, J., Lissenberg, C. J., O'Driscoll, B., Karakas, O., Falloon, T., Klimentyeva, D. N., & Ulmer, P. (2018). Partial melting of lower oceanic crust gabbro: Constraints from poikilitic clinopyroxene primocrysts. *Frontiers in Earth Science*, *6*, 15. https://doi.org/10.3389/feart.2018.00015

Lissenberg, C. J., & Dick, H. J. B. (2008). Melt-rock reaction in the lower oceanic crust and its implications for the genesis of mid-ocean ridge basalt. *Earth and Planetary Science Letters*, *271*(1–4), 311–325. https://doi.org/10.1016/j.epsl.2008.04.023

Lissenberg, C. J., & MacLeod, C. J. (2016). A reactive porous flow control on mid-ocean ridge magmatic evolution. *Journal of Petrology*, *57*(11–12), 2195–2220. https://doi.org/10.1093/petrology/egw074

Lissenberg, C. J., MacLeod, C. J., Howard, K. A., & Godard, M. (2013). Pervasive reactive melt migration through fast-spreading lower oceanic crust (Hess Deep, equatorial Pacific Ocean). *Earth and Planetary Science Letters*, *361*, 436–447. https://doi.org/10.1016/j.epsl.2012.11.012

Lissenberg, J. C., MacLeod, C. J., & Bennett, E. N. (2019). Consequences of a crystal mush-dominated magma plumbing system: A mid-ocean ridge perspective. *Philosophical Transactions of the Royal Society A: Mathematical, Physical and Engineering Sciences*, *377*(2139), 20180014. https://doi.org/10.1098/rsta.2018.0014

MacLeod, C. J., Dick, H. J. B., Blum, P., Abe, N., Blackman, D. K., Bowles, J. A., et al. (2017a). Hole 1105A redescription. *Proceedings of the Ocean Drilling Program*, *360*. https://doi.org/10.14379/iodp.proc.360.104.2017

MacLeod, C. J., Dick, H. J. B., Blum, P., Abe, N., Blackman, D. K., Bowles, J. A., et al. (2017b). Site U1473. *Proceedings of the Ocean Drilling Program*, *360*. https://doi.org/10.14379/iodp.proc.360.103.2017

Magde, L. S., Barclay, A. H., Toomey, D. R., Detrick, R. S., & Collins, J. A. (2000). Crustal magma plumbing system within a segment of the slow-spreading MAR, 35°N. *Earth and Planetary Science Letters*, *79*, 799.

Mainprice, D., Bachmann, F., Hielscher, R., & Schaeben, H. (2014). Descriptive tools for the analysis of texture projects with large datasets using MTEX : Strength, symmetry and components. *Geological Society, London, Special Publications*, *409*(1), 251–271. https://doi.org/10.1144/SP409.8

Mainprice, D., & Silver, P. G. (1993). Interpretation of SKS-waves using samples from the subcontinental lithosphere. *Physics of the Earth and Planetary Interiors*, *78*(3–4), 257–280. https://doi.org/10.1016/0031-9201(93)90160-B

Meyer, P. S., Dick, H. J. B., & Thompson, G. (1989). Cumulate gabbros from the Southwest Indian Ridge, 54°S–7°16′E: Implications for magmatic processes at a slow spreading ridge. *Contributions to Mineralogy and Petrology*, *103*(1), 44–63. https://doi.org/10.1007/BF00371364

Mock, D., Neave, D. A., Müller, S., Garbe-Schönberg, D., Namur, O., Ildefonse, B., & Koepke, J. (2020). Formation of igneous layering in the lower oceanic crust from the Samail Ophiolite, Sultanate of Oman. *Journal of Geophysical Research: Solid Earth*, *126*. https://doi.org/10.1029/2020jb019573

Morales, L. F. G., Boudier, F., & Nicolas, A. (2011). Microstructures and crystallographic preferred orientation of anorthosites from Oman ophiolite and the dynamics of melt lenses. *Tectonics*, *30*(2). https://doi.org/10.1029/2010TC002697

Namur, O., Abily, B., Boudreau, A. E., Blanchette, F., Bush, J. W. M., Ceuleneer, G., et al. (2015). Igneous layering in basaltic magma chambers. In B. Charlier, O. Namur, R. Latypov, & C. Tegner (Eds.), *Layered intrusions* (pp. 1–748). Springer. https://doi.org/10.1007/978-94-017-9652-1

Naslund, H. R., & McBirney, A. R. (1996). Mechanisms of formation of igneous layering. *Developments in Petrology*, *15*(C), 1–43. https://doi.org/10.1016/S0167-2894(96)80003-0

Natland, J. H., & Dick, H. J. B. (2001). Formation of the lower ocean crust and the crystallization of gabbroic cumulates at a very slowly spreading ridge. *Journal of Volcanology and Geothermal Research*, *110*(3–4), 191–233. https://doi.org/10.1016/S0377-0273(01)00211-6

Natland, J. H., & Dick, H. J. B. (2002). Stratigraphy and composition of gabbros drilled in ODP Hole 735B, SWIR: A synthesis of geochemical data. *Proceedings of the Ocean Drilling Program*, *176*, 1–69.

Natland, J. H., Meyer, P. S., Dick, H. J. B., & Bloomer, S. H. (1991). Magmatic oxides and sulfides in gabbroic rocks from Hole 735B and the later development of the liquid line of descent. *Proceedings of the Ocean Drilling Program, Scientific Results*, *118*(3), 75–111. https://doi.org/10.2973/odp.proc.sr.118.163.1991

Navon, O., & Stopler, E. (1985). Geochemical consequences of melt percolation: The upper mantle as a chromatographic melt column. *Journal of Geology*, *93*(6).

Nguyen, D. K., Morishita, T., Soda, Y., Tamura, A., Ghosh, B., Harigane, Y., et al. (2018). Occurrence of felsic rocks in oceanic gabbros from IODP Hole U1473A: Implications for evolved melt migration in the lower oceanic crust. *Minerals*, *8*, 583. https://doi.org/10.3390/min8120583

Niu, Y., Gilmore, T., Mackie, S., Greig, A., & Bach, W. (2002). Mineral chemistry, whole-rock compositions, and petrogenesis of Leg 176 gabbros: Data and discussion. *Proceedings of the Ocean Drilling Program, Scientific Results*, *176*. https://doi.org/10.2973/odp.proc.sr.176.011.2002

O'Hara, M. J. (1965). Primary magmas and the origin of basalts. *Scottish Journal of Geology*, *1*(1), 19–40. https://doi.org/10.1144/sjg01010019

Pearce, N. J. G., Perkins, W. T., Westgate, J. A., Gorton, M. P., Jackson, S. E., Neal, C. R., & Chenery, S. P. (1997). A compilation of new and published major and trace element data for NIST SRM 610 and NIST SRM 612 glass reference materials. *Geostandards Newsletter*, *21*(1), 115–144. https://doi.org/10.1111/j.1751-908X.1997.tb00538.x

Quick, J. E., & Denlinger, R. P. (1993). Ductile deformation and the origin of layered gabbro in ophiolites. *Journal of Geophysical Research: Solid Earth*, *98*(B8), 14015–14027. https://doi.org/10.1029/93jb00698

Rampone, E., Piccardo, G. B., & Hofmann, A. W. (2008). Multi-stage melt-rock interaction in the Mt. Maggiore (Corsica, France) ophiolitic peridotites: Microstructural and geochemical evidence. *Contributions to Mineralogy and Petrology*, *156*(4), 453–475. https://doi.org/10.1007/s00410-008-0296-y

Ross, D. K., & Elthon, D. (1997). Cumulus and postcumulus crystallization in the oceanic crust: Major- and trace-element geochemistry of Leg 153 gabbroic rocks. *Proceedings of the Ocean Drilling Program, Scientific Results*, *153*, 333–353. https://doi.org/10.2973/odp.proc.sr.153.023.1997

Rubin, K. H., & Sinton, J. M. (2007). Inferences on mid-ocean ridge thermal and magmatic structure from MORB compositions. *Earth and Planetary Science Letters*, *260*(1–2), 257–276. https://doi.org/10.1016/j.epsl.2007.05.035

Ryan, W. B. F., Carbotte, S. M., Coplan, J. O., Hara, S. O., Melkonian, A., Arko, R., et al. (2009). Global multi-resolution topography synthesis. *Geochemistry, Geophysics, Geosystems*, *10*. https://doi.org/10.1029/2008GC002332

Sanfilippo, A., Macleod, C. J., Tribuzio, R., Lissenberg, C. J., & Zanetti, A. (2020). Early-stage melt-rock reaction in a cooling crystal mush beneath a (IODP Hole U1473A, Atlantis Bank, Southwest Indian Ridge). *Frontiers in Earth Science*, *8*, 1–21. https://doi.org/10.3389/feart.2020.579138

Sanfilippo, A., & Tribuzio, R. (2011). Melt transport and deformation history in a nonvolcanic ophiolitic section, northern Apennines, Italy: Implications for crustal accretion at slow spreading settings. *Geochemistry, Geophysics, Geosystems*, *12*(7). https://doi.org/10.1029/2010GC003429

Sanfilippo, A., & Tribuzio, R. (2013). Building of the deepest crust at a fossil slow-spreading centre (Pineto gabbroic sequence, Alpine Jurassic ophiolites). *Contributions to Mineralogy and Petrology*, *165*(4), 705–721. https://doi.org/10.1007/s00410-012-0831-8

Sanfilippo, A., Tribuzio, R., & Tiepolo, M. (2014). Mantle-crust interactions in the oceanic lithosphere: Constraints from minor and trace elements in olivine. *Geochimica et Cosmochimica Acta*, *141*, 423–439. https://doi.org/10.1016/j.gca.2014.06.012

Sanfilippo, A., Tribuzio, R., Tiepolo, M., & Berno, D. (2015). Reactive flow as dominant evolution process in the lowermost oceanic crust: Evidence from olivine of the Pineto ophiolite (Corsica). *Contributions to Mineralogy and Petrology*, *170*(4), 1–12. https://doi.org/10.1007/s00410-015-1194-8

Satsukawa, T., Ildefonse, B., Mainprice, D., Morales, L. F. G., Michibayashi, K., & Barou, F. (2013). A database of plagioclase crystal preferred orientations (CPO) and microstructures-implications for CPO origin, strength, symmetry and seismic anisotropy in gabbroic rocks. *Solid Earth*, *4*(2), 511–542. https://doi.org/10.5194/se-4-511-2013

Shipboard Scientific Party. (1989). Shipboard Scientific Party 2 Hole 735A. *Proceedings of the Ocean Drilling Program, Scientific Results*, *118*, 89–222.

Singh, S. C., Crawford, W. C., Carton, H., Seher, T., Combier, V., Cannat, M., et al. (2006). Discovery of a magma chamber and faults beneath a Mid-Atlantic Ridge hydrothermal field. *Nature*, *442*(7106), 1029–1032. https://doi.org/10.1038/nature05105

Sinha, M. C., Constable, S. C., Peirce, C., White, A., Heinson, G., MacGregor, L. M., & Navin, D. A. (1998). Magmatic processes at slow spreading ridges: Implications of the RAMESSES experiment at 57°45′N on the Mid-Atlantic Ridge. *Geophysical Journal International*, *135*(3), 731–745. https://doi.org/10.1046/j.1365-246X.1998.00704.x

Sinha, M. C., Navin, D. A., Macgregor, L. M., Constable, S., Peirce, C., White, A., et al. (1997). Evidence for accumulated melt beneath the slow-spreading Mid-Atlantic Ridge. *Philosophical Transactions of the Royal Society A: Mathematical, Physical and Engineering Sciences*, *355*(1723), 233–253. https://doi.org/10.1098/rsta.1997.0008

Suhr, G., Hellebrand, E., Johnson, K., & Brunelli, D. (2008). Stacked gabbro units and intervening mantle: A detailed look at a section of IODP Leg 305, Hole U1309D. *Geochemistry, Geophysics, Geosystems*, *9*(10). https://doi.org/10.1029/2008GC002012

Tegner, C., Wilson, J. R., & Brooks, C. K. (1993). Intraplutonic quench zones in the Kap-Edvard-Holm-layered-gabbro-complex, east Greenland. *Journal of Petrology*, *34*(4), 681–710. https://doi.org/10.1093/petrology/34.4.681

van Achterbergh, E., Griffin, W. L., Ryan, C. G., O'Reilly, S. Y., Pearson, N. J., Kivi, K., & Doyle, B. J. (2004). Melt inclusions from the deep Slave lithosphere: Implications for the origin and evolution of mantle-derived carbonatite and kimberlite. *Lithos*, *76*(1–4), 461–474. https://doi.org/10.1016/j.lithos.2004.04.007

Vernières, J., Godard, M., & Bodinier, J.-L. (1997). A plate model for the simulation of trace element fractionation during partial melting and magma transport in the Earth's upper mantle. *Journal of Geophysical Research: Solid Earth*, *102*(B11), 24771–24784. https://doi.org/10.1029/97jb01946

Villiger, S., Müntener, O., & Ulmer, P. (2007). Crystallization pressures of mid-ocean ridge basalts derived from major element variations of glasses from equilibrium and fractional crystallization experiments. *Journal of Geophysical Research*, *112*(1), 1–18. https://doi.org/10.1029/2006JB004342

Villiger, S., Ulmer, P., & Müntener, O. (2007). Equilibrium and fractional crystallization experiments at 0.7 GPa; the effect of pressure on phase relations and liquid compositions of tholeiitic magmas. *Journal of Petrology*, *48*(1), 159–184. https://doi.org/10.1093/petrology/egl058

Yang, A. Y., Wang, C., Liang, Y., & Lissenberg, C. J. (2019). Reaction between mid-ocean ridge basalt and lower oceanic crust: An experimental study. *Geochemistry, Geophysics, Geosystems*, *20*(9), 4390–4407. https://doi.org/10.1029/2019GC008368

Zhang, W.-Q., Liu, C.-Z., & Dick, H. J. B. (2021). Evidence for multi-stage melt transport in the lower ocean crust: The Atlantis Bank Gabbroic Massif (IODP Hole U1473A, SW Indian Ridge). *Journal of Petrology*, *61*(9). https://doi.org/10.1093/petrology/egaa082